Study of the ALICE Investigator chip in view of the requirements at CLIC

D. Dannheim[*], A. Fiergolski[*], J.v. Hoorne[*], D. Hynds[*], W. Klempt[*], M. Munker[1)*†],
A. Nürnberg[*], K. Sielewicz[*], W. Snoeys[*]

[*] *CERN, Switzerland,* [†] *University of Bonn, Germany*

Abstract

CLIC is an option for a future high energy linear e^+e^- collider at CERN in the post-LHC era. The CLIC machine is designed to reach centre-of-mass energies ranging from a few hundred GeV up to 3 TeV. To achieve high precision measurements, e.g. of the Higgs-width, challenging requirements are imposed on the CLIC detector. A single point tracking resolution of $7\,\mu$m and a material budget of $1\text{-}2\,\%X_0$ per layer are required for the tracker. Moreover, to suppress background hits from beam-beam interactions, a precise time slicing of hits of $10\,$ns is needed. To address these requirements, a large area silicon tracker is foreseen for the detector at CLIC. In this context, integrated technologies are promising candidates to achieve large scale production and low material budget. The Investigator chip is a test chip developed for the ALICE Inner Tracking System upgrade, implemented in a $180\,$nm CMOS process on a high resistivity substrate. It contains various test-matrices with analogue functionality, which are read out by external sampling ADCs. This paper introduces the process and technology of the Investigator chip, describes the data taking and reconstruction setup and presents results on spatial and timing resolutions, as well as efficiency measurements, for a pixel pitch of $28\,\mu$m.

This work was carried out in the framework of the CLICdp collaboration

[1]Corresponding author:
  magdalena.munker@cern.ch

1. Introduction

CLIC is a future option of a linear e^+e^- collider in the post-LHC era at CERN [1–4]. A centre-of-mass energy up to $3\,\mathrm{TeV}$ is planned to be reached at CLIC. To achieve high precision measurements, demanding requirements are imposed on the CLIC detector [5]. A single point resolution of $7\,\mu\mathrm{m}$ and a material budget of $1\text{-}2\%\mathrm{X}_0$ per layer are needed for the tracker [5]. Furthermore, a time slicing of $10\,\mathrm{ns}$ is required for the hits, to suppress out-of-time background from beam-beam interactions [5, 6]. To address these requirements, a large area silicon tracker with a surface of $\sim 100\,\mathrm{m}^2$ is proposed for the CLIC detector [5]. Different technologies are currently under investigation in a broad silicon detector R&D programme for CLIC. The use of well-known technologies, such as planar strip sensors wire bonded to a separate readout ASIC, is not feasible for small strips (down to $1\,\mathrm{mm}$ in the inner tracker layers [5, 6]). Moreover, the separated readout ASICs would result in additional material. Thus, monolithic technologies are attractive candidates in view of large surface and low material budget.

The ALPIDE chip, a fully monolithic pixel-chip, has been developed for the ALICE Inner Tracking System (ITS) upgrade [7, 8] in a High-Resistivity (HR) $180\,\mathrm{nm}$ CMOS technology. Using the same underlying process as for the ALPIDE chip, the Investigator test-chip, has been produced for the ALICE ITS upgrade. The process of the Investigator test-chip has been modified to achieve a full lateral depletion of the sensor volume, being attractive for the CLIC tracker to achieve a fast timing capability. Moreover, it contains various test-pixel matrices with different pixel layouts and analogue functionality, which are implemented for various matrices, allowing for a comparison of the analogue performance and optimisation of future designs in this technology. The different pixel designs have been optimised e.g. to minimise the capacitance of the collection diode to the order of a few fF. By this, a low analogue power consumption and a fast timing capability have been achieved, making the Investigator an interesting candidate to study for the CLIC tracker.

To study the Investigator performance, various test-beam campaigns have been performed at the CERN SPS, using the CLICdp Timepix3 telescope [9]. A calibration has been performed and the noise has been characterised to interpret the test-beam results. Test-beam results of timing resolution, spatial resolution and detection efficiency are presented for a pixel pitch of $28\,\mu\mathrm{m}$, and discussed with emphasis on the requirements at CLIC.

2. Investigator chip

The Investigator chip consists of several sections with different pixel layouts, so called mini-matrices. Several geometrical and electronics parameters have been changed for the various pixel layouts, aiming at an optimisation of the pixel layout e.g. in terms of efficiency, spatial and timing resolution. Each mini-matrix consists of 10×10 pixels, with the 8×8 innermost pixels being read out.

2.1. Pixel layout

The cross-section of the used HR $180\,\mathrm{nm}$ CMOS process is presented in Figure 1. The process makes use of a deep planar pn-junction, being created between a HR ($1\text{-}8\,\mathrm{k}\Omega\,\mathrm{cm}$) P-type epitaxial layer and an N-layer.

Each pixel consists of an N-well collection diode and CMOS circuitry. The NMOS transistor is embedded in a P-well and the PMOS transistor is embedded in a separate N-well. The N-well from the PMOS transistor is shielded by a deep P-well, to prevent an efficiency loss caused by attracting signal charge to the PMOS N-well. As shown in Figure 1, this deep P-well continues under the P-well of the NMOS transistor and the resulting P-well structure forms a ring around the N-well collection diode. A bias voltage is applied to terminals in this P-type structure and connected via non-depleted regions at the Investigator matrix edges to the backside of the chip.
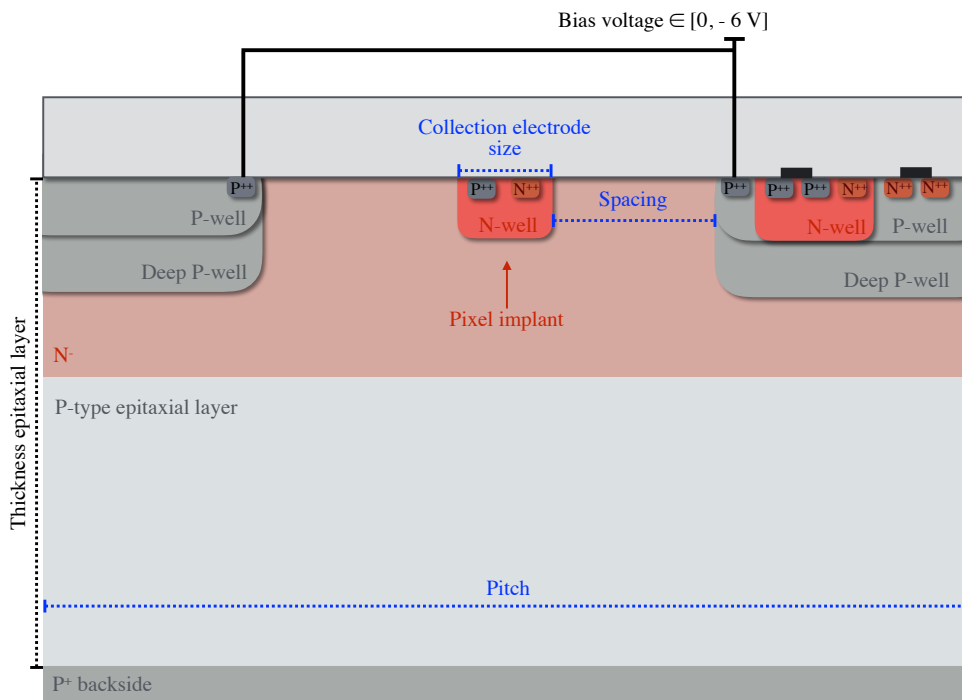
Bias voltage $\in$ [0, - 6 V]

Figure 1: Cross-section (not to scale) of the HR 180 nm CMOS process used for the fabrication of the Investigator chip. The schematic represents one unit cell, of the periodic pixel matrix.

When applying a negative bias voltage, a depleted region starts to evolve from pn-junctions around the P-wells, as well as from the deep planar pn-junction, depleting the N- and epitaxial-layer. As shown in Figure 1, a pn-junction is also created between the N^{++} implants of the NMOS transistor and the P-well ring, being reversed biased by the bias voltage applied to the terminals in the P-well ring [10]. To avoid breakdowns of this pn-junction, the bias voltage is limited to -6 V. Moreover, a voltage of 1.8 V is applied to terminals in the N-well of the PMOS transistors, to reverse bias them. In the N-well collection diode P^{++} terminals are implanted to apply a reset pulse, as described in the next Chapter 2.2.

Different mini-matrices contain pixels of various pitch, collection electrode sizes and spacings (see blue parameters in Figure 1).

2.2. Charge collection and charge sharing

When a particle traverses the sensor material, electron hole pairs are created and move either randomly (diffusion), or according to the electric field in the sensor (drift). Electrons drift to the N-well collection diodes, whereas holes drift to the P-wells or the P-type backside. The amount of charge induced on a single readout electrode depends on various parameters like the exact formation of the electric field in the sensor, the pixel size and the position where the charge is created in the sensor.

If a particle instead traverses the sensor in the centre of a pixel it is more likely that only the readout electrode of this pixel collects charge. If the particle traverses the sensor close to the pixel borders it is more likely that several pixels collect charge, i.e. the charge is shared between the pixels, in the following referred to as *charge sharing*.

Each pixel contains a source follower which converts the charge Q on the diode capacitance C to a voltage U = Q/C, as shown in Figure 2. As a consequence, a particle traversing the sensor manifests itself in a measured voltage drop.
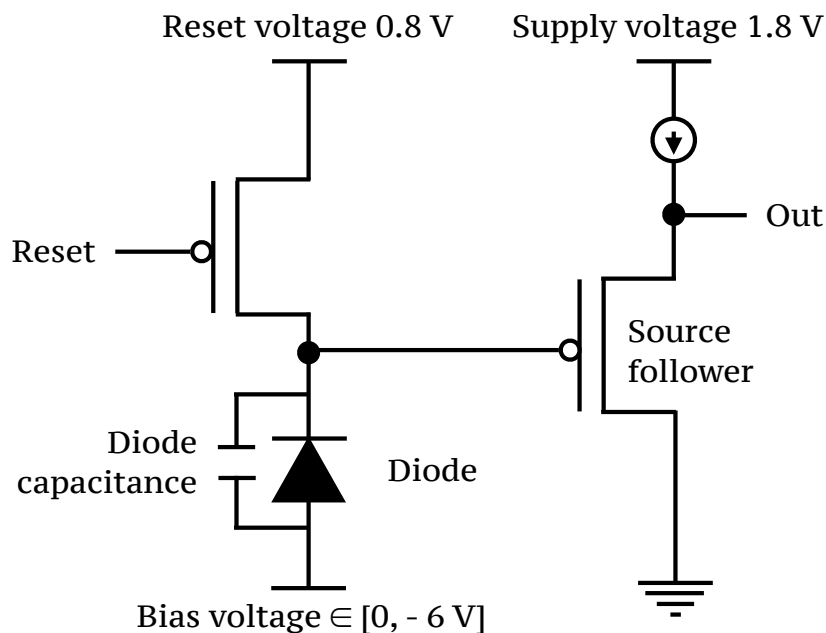
Figure 2: Simplified single pixel schematic.

Accordingly, the small input capacitance of the N-well collection diode of a few fF [11] results in a large voltage drop. Thus, low power is needed to amplify the signal, leading to a low analogue power consumption of the Investigator. With a reset pulse, sent to the P^{++} terminals in the N-well collection diode, the diode capacitance C gets discharged, and the voltage U is returns back to the pedestal.

2.3. INvestigator ReadOut System (INVROS)

Being a test-chip, the Investigator does not comprise the digital logic on chip, and a dedicated readout system, the INVROS (INvestigator ReadOut System), has been designed for the Investigator to record the full analogue data for each pixel [10].

Due to a limited number of output buffers in the periphery of the Investigator, only one mini-matrix can be read out at a time. Selecting one mini-matrix, these pixels are read out by connecting the output of the source follower to a dedicated output buffer at the periphery. The INVROS uses one Analogue to Digital Converter (ADC) per readout pixel, sampling the pixel front end output with a frequency of 65 MHz and 14-bit resolution (AD9249 [12]). Moreover, the INVROS provides the reset signal, the 1.8 V for the reverse bias of the PMOS transistors and the supply voltage to corresponding input pads on the Investigator periphery. The reset pulse is sent with an adjustable period to all 10×10 pixels, regardless if a voltage drop was recorded or not.

The time window between two reset pulses consists of two windows, as illustrated in Figure 3. To avoid the reset pulse from faking signal in the sensor[2], one time window (denoted *Inactive window* in Figure 3) is defined $0.15\,\mu s$ before the start of the reset pulse. The window size is tuned to a length of $12.4\,\mu s$, after which the output is stabilised and the voltage has returned to its pedestal value, see Figure 3. Data recorded in this time window are rejected by the INVROS and result in dead times of the Investigator chip. After this time, the INVROS stores the data observed by the Investigator for an *Active window* of 1024 time samples (see Figure 3), corresponding to $15.75\,\mu s$. An additional $0.15\,\mu s$ of dead time occurs between each recording cycle.

---

[2] As shown in Figure 3, the reset pulse results in a negative voltage drop, mimicking a voltage drop created from a particle traversing the sensor.
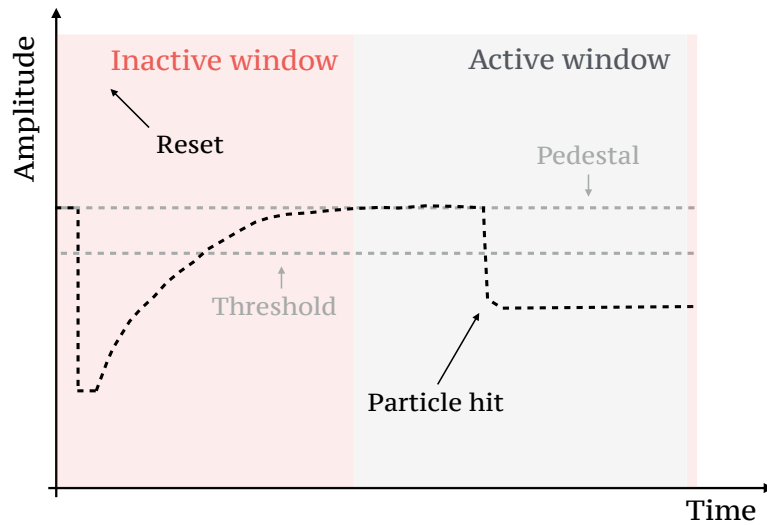
Figure 3: Simplified schematic of Investigator waveform for one time cycle (not to scale), as discussed in the text.

If a voltage drop below a certain *triggering threshold* value has been observed in at least one pixel during the Active window, the full frame of the amplitudes of the 8×8 read out pixels gets recorded. The triggering threshold is determined during data taking and is set individually for each pixel such that it corresponds to the same ratio of threshold/noise. During the time the INVROS sends the recorded data to the computer, additional particle hits seen by the Investigator are not recorded by the computer. This results in additional dead time of the Investigator readout system in the order of a few ms after a particle hit.

Overall, the previously discussed dead times are attributed to the way the analogue circuitry is implemented in the Investigator pixel (dead time due to reset pulse) and the used external readout (dead times during data transverse between external readout board and computer). An assessment of the dead times is important to understand the data taking rate during test-beam, with the used setup. However, no conclusions can be drawn for a fully integrated design for the CLIC tracker.

3. Reconstruction of Investigator pixel waveforms

A characterisation with source and test-beam measurements has been performed. The basic procedure to reconstruct the Investigator pixel waveforms is described in the following chapter.

The study was done for a mini-matrix with a pitch of $28\,\mu$m, a spacing of $2\,\mu$m and a collection electrode size of $3\,\mu$m (located on an Investigator chip with an epitaxial layer thickness of $25\,\mu$m). The pitch was selected according to a rough estimate of the desired spatial resolution. Moreover, all geometrical and electrical parameters have been selected to match the design parameters of the ALPIDE chip [7], to achieve a better comparison of the results.

3.1. Common mode noise correction

The *pedestal amplitude* is defined as the readout amplitude value, if no particle is traversing the sensor. A systematic deviation from the pedestal amplitude (in the following referred to as *common mode noise*) has been observed in all readout Investigator amplitudes. This common mode noise has the same form for each pixel in one readout-frame. In the further analysis a threshold is applied on single pixel level

with a constant threshold/noise ratio, referred to as *analysis threshold*. The noise, defined as the RMS of the pedestal amplitudes (see Section 5), would be shifted by the common mode noise to higher values. A rise in noise will consequently lead to an increase of this threshold, ultimately leading to a decreased hit position reconstruction as further discussed in Section 3. Thus, the common mode noise needs to be calculated and subtracted from the single pixel waveforms.

The waveform of the common mode noise is extracted from pixels without a particle hit. A particle hit is defined as the voltage drop caused by a particle traversing the sensor and identified by studying the difference in amplitude between the first time sample and the last time sample. To find pixels with no particle hit for the common mode noise analysis, this difference is required to be smaller than a value of 20 ADC. This value has been selected to be well above the common mode noise amplitude but below the expected amplitude drop from a particle hit. Further, the pedestal value is calculated for each pixel by looping over a few hundred Investigator frames and extracting the average amplitude for pixels without a particle hit. After subtracting the pedestal from each single pixel waveform, the mean waveform of the common mode noise in a specific frame is obtained by averaging the waveform of all pixels without a particle hit. A typical common mode noise waveform (averaged over all pixels with no particle hit in a readout frame) is presented in Figure 4 for a bias voltage[3] of $-6\,\mathrm{V}$.
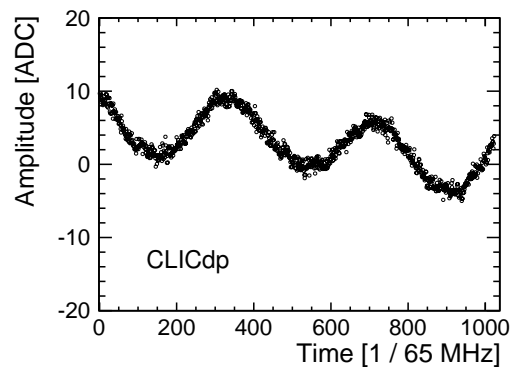

Figure 4: Typical example of a calculated common mode noise waveform.

The waveform of each single pixel is then corrected by subtracting the obtained mean common mode noise waveform of the specific readout frame. Waveforms of an example pixel with no particle hit are shown before and after the common mode noise correction for a bias voltage of $-6\,\mathrm{V}$ (see Figure 5).

In Figure 6 waveforms of an example pixel with a particle hit are shown before and after the common mode noise correction for a bias voltage of $-6\,\mathrm{V}$.

3.2. Hit time and amplitude

A typical waveform of a pixel with a particle hit is presented in Figure 7, showing the recorded amplitude for the time samples around a particle hit. A search for a particle hit is performed for each pixel, by looping through all time samples. The distance in amplitude is computed for each time sample i in relation to the third sample before $i - 3$, as indicated in Figure 7. This is motivated by the fact that at most 2 readout samples lie within the slope of the waveform with a particle hit. The time sample pair with a maximum of this distance in amplitude is identified, and a first estimate of the hit time within the readout window is set to the third sample before.

To estimate the amplitude drop created by a particle hit (the signal) 10 time samples around the estimated hit time from above are masked.

---

[3]The common mode is characterised for different bias voltages, see details in Section 4.
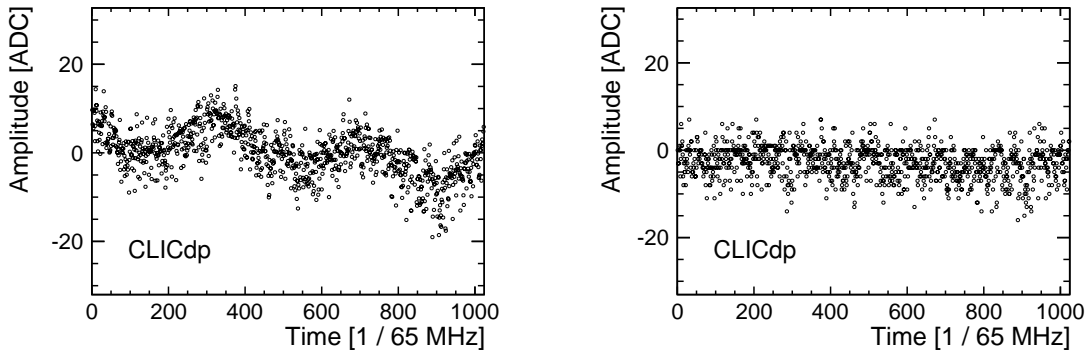
Figure 5: Example of a waveform of a pixel without a particle hit *before* (left) *after* (right) the common mode noise correction.
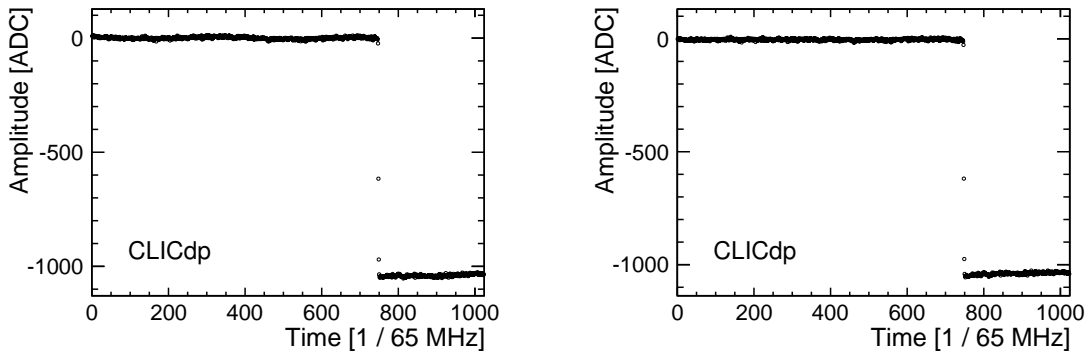

Figure 6: Example of a waveform of a pixel with a particle hit *before* (left) *after* (right) the common mode noise correction.
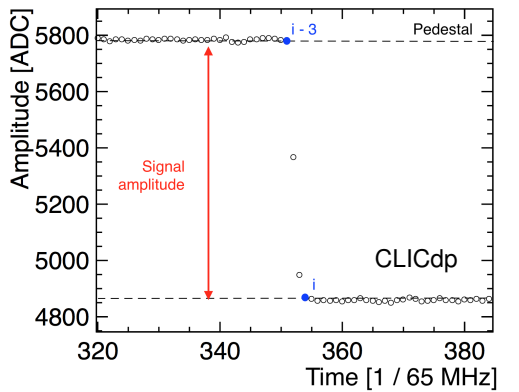

Figure 7: Illustration of the procedure to estimate the particle hit time within the readout window.
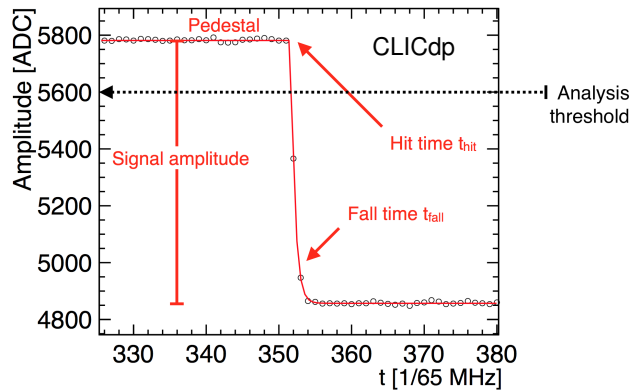
Figure 8: Fit (red line) of a constant function with an exponential decay to the single pixel waveform.

The signal height is defined as the difference between averages of the remaining time samples on each side of the mask[4]. The noise is defined as the RMS of the amplitude values in the non-masked regions.

---

[4] If a particle hit happens in the first or last 10 samples of the readout window (10 samples correspond to $0.15\,\mu s$, being $< 1\,\%$ of the $15.75\,\mu s$ long active window), the Investigator hit is not reconstructed by the analysis. This does not result in a loss

To remove noise contributions to the signal, an analysis threshold is applied requiring the signal to be larger than N times the noise.

A fit to the single pixel waveforms is performed, using the estimate of the hit time and signal as start values. This is important to achieve a better precision on the hit time as the procedure described above is limited by the sampling frequency of 65 MHz. Each single pixel waveform is fitted with the following function f(t):

$$f(t) = \begin{cases} \text{Pedestal}, & if\ t \le t_{hit} \\ \text{Pedestal} + (\text{Signal Amplitude}) \cdot (e^{-(t-t_{hit})/t_{fall}} - 1), & if\ t > t_{hit}. \end{cases} \quad (1)$$

The time constant of the exponential drop is characterised by the fall time constant t_{fall} (see Figure 8). Free parameters of the fit are the pedestal and the signal amplitude, as well as the hit time t_{hit} and the fall time constant t_{fall}. The start value for the fall time constant t_{fall} of the fit was set to two time samples, being motivated by the typical waveform, as shown for example in Figure 7 and 8. The χ^2/ndof for a few thousands of fits to single pixel waveforms, is presented in Figure 9.
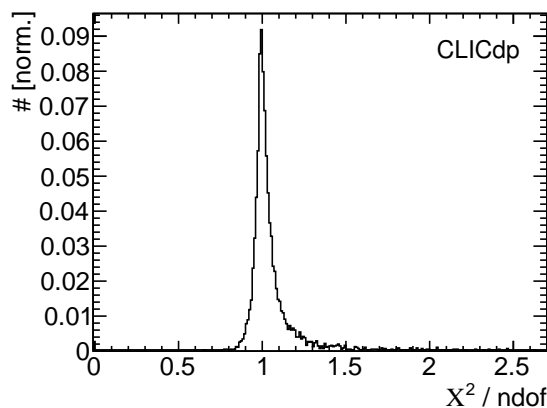

Figure 9: χ^2/ndof of the waveform fits in equation 1.

4. Calibration

Calibration data have been recorded for the Investigator chip using an ^{55}Fe-source in laboratory measurements [10]. This source has two very close-by X-ray emission lines at 5.9 keV (K-alpha lines) and one X-ray emission line at 6.5 keV (K-beta line). The K-alpha lines have a combined probability of 24.4 % and result in an energy deposit of 1639 e$^-$ in silicon [13]. The K-beta line has a probability of 2.85 % and result in an energy deposit of 1806 e$^-$ in silicon [13]. Local charge deposits in the sensor are expected from the absorption of the photons from the X-ray emission lines, resulting in a peak of the measured signal around the energy of the emission lines. The data have been reconstructed as described in Section 3. To avoid a bias of the calibration due to charge sharing effects, the threshold during the analysis is set to very low values of two times above the noise and only clusters consisting of a single pixel are considered.

Different bias voltages change the depleted region in the sensor and therefore the sensor capacitance: the smaller the depleted volume in a sensor, the larger the sensor capacitance. A different sensor capacitance therefore results in a different capacitive load and a different gain factor of the in-pixel CMOS

---

of efficiency since the first and last μs of the active window are masked, as discussed later in Section 6.4.5.

transistors (see Section 2.2). For this reason the calibration has been performed separately for each bias voltage.

A Gaussian was fitted to the peak at $1639\,e^-$, while the peak at $1806\,e^-$ was excluded due to limited statistics. Thus, the calibration was performed at a single energy point, assuming a linear response of the pixel ADCs for different energies. Due to small pixel by pixel gain fluctuations (see Appendix A) a global calibration has been performed by fitting a Gaussian to the $1639\,e^-$ emission line of the combined statistics of all pixels (see Figure 10 - 12).
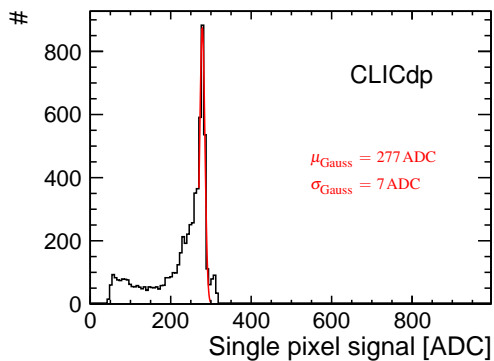
Figure 10: Single pixel cluster ^{55}Fe-spectrum for a bias voltage of $-1\,\mathrm{V}$.
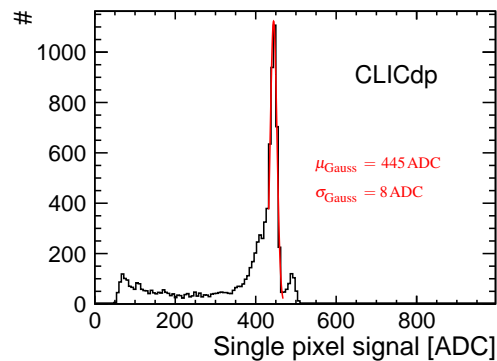
Figure 11: Single pixel cluster ^{55}Fe-spectrum for a bias voltage of $-3\,\mathrm{V}$.
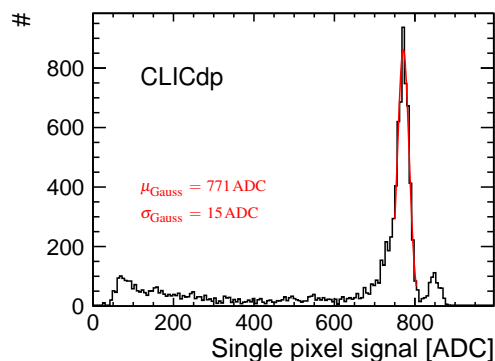
Figure 12: Single pixel cluster ^{55}Fe-spectrum for a bias voltage of $-6\,\mathrm{V}$.

Beside the peaks expected from the two emission lines, the combined spectra show a tail to lower energies. This can either be attributed to photon conversion in the substrate or charge sharing effects. Photon conversion in the substrate is expected since the epitaxial layer thickness of the studied Investigator is $25\,\mu$m, whereas the attenuation length of the emission lines are $29\,\mu$m (K-alpha lines) and $37\,\mu$m (K-beta line) [13]. Charge sharing effects can play a role if charge shared to neighbouring pixels falls below the threshold.

The extracted mean values from the Gaussian fits can be used to calculate the calibration factor CF

$$\mathrm{CF} = 1639\,[e^-]\,/\,\mathrm{Mean_{Gauss}}\,[\mathrm{ADC}], \tag{2}$$

by which the measured signal amplitude, noise and threshold need to be scaled to be converted into a scale in units of electrons. The CF for different bias voltages are presented in Figure 13. Larger CF's have been measured for lower absolute bias voltages, being consistent with the expected lower gain at lower absolute voltages due to a larger sensor capacitance.
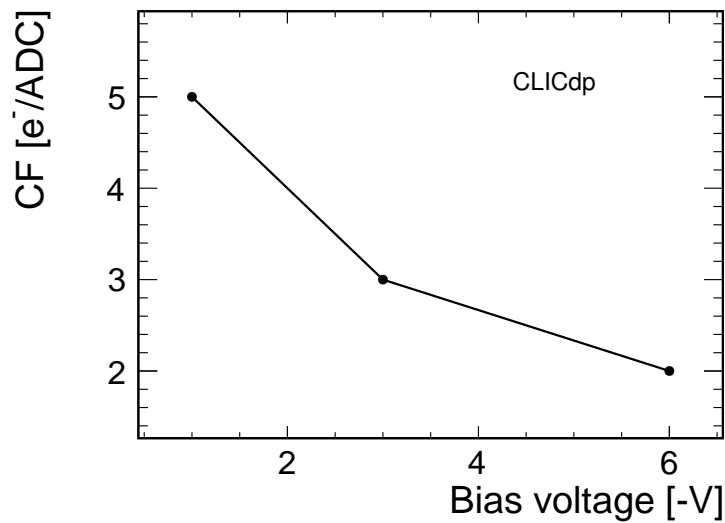
Figure 13: Calibration factors, defined as $\text{CF} = 1639\,[\text{e}^-]\,/\,\text{Mean}_{\text{Gauss}}[\text{ADC}]$, versus bias voltage. The mean values of the Gaussian fits $\text{Mean}_{\text{Gauss}}$ are taken from Figure 10 - 12.

5. Noise characteristics

5.1. Common mode noise and leakage current

Examples of typical common mode noise waveforms are presented in Figure 14 - 16 for different bias voltages. The common mode noise is composed of two components: a drift of the waveform to lower amplitudes for later times, which is attributed to a leakage current, and an overlaying oscillation. To determine the value of the leakage current, the frequency and amplitude of the oscillation, a fit of the function f(t) (see red line in Figure 14 - 16) has been performed:

$$
\begin{aligned}
\text{f(t)} = {} & -\text{Drift}\,[\text{ADC} \cdot 65\text{MHz}] \cdot \text{t}\,[1/65\text{MHz}] \\
& -\text{Amplitude}\,[\text{ADC}] \cdot \sin(2\pi \cdot \text{Frequency}\,[65\text{MHz}] \cdot \text{t}\,[1/65\text{MHz}] + \text{Phase}). \\
& +\text{Offset}\,[\text{ADC}]
\end{aligned}
\tag{3}
$$

Using the CF one can calculate the leakage current

$$
\begin{aligned}
\text{I}_{\text{Leakage}}\,[\text{A}] &= \text{CF} \cdot \text{Drift}\,[\text{e}^- \cdot 65\,\text{MHz}] \\
&= \text{CF} \cdot 1.60217646 \cdot 10^{-19} \cdot \text{Drift} \cdot 65 \cdot 10^6\,[\text{A}].
\end{aligned}
\tag{4}
$$

The amplitude and frequency of the common mode noise are presented in Figure 17 for different bias voltages. The amplitude of the common mode noise decreases for lower absolute bias voltages, which is consistent with the observed lower gain for lower voltages (see Figure 13).

The frequency of the common mode noise is not affected by the applied bias voltage. A possible explanation of this oscillation might be a noise from the power supply. The leakage current versus bias voltage is presented in Figure 18. The values of the leakage current are in the range of 10^{-13} A. Higher leakage current values have been measured for a higher absolute bias voltage, as expected from the larger depletion region in the sensor.
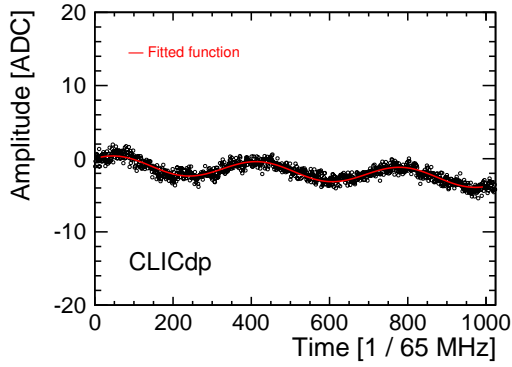
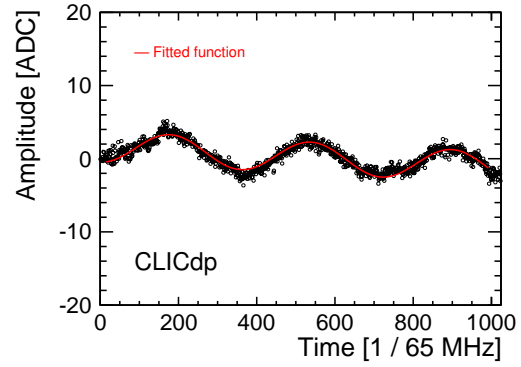Figure 14: Common mode noise waveform for a bias voltage of $-1\,\text{V}$.

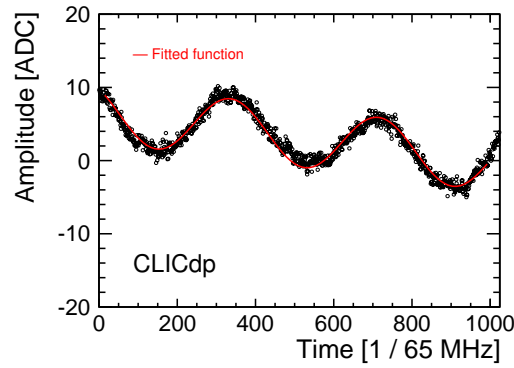Figure 15: Common mode noise waveform for a bias voltage of $-3\,\text{V}$.

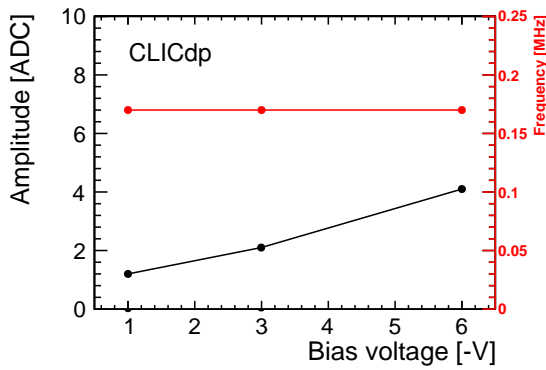Figure 16: Common mode noise waveform for a bias voltage of $-6\,\text{V}$.

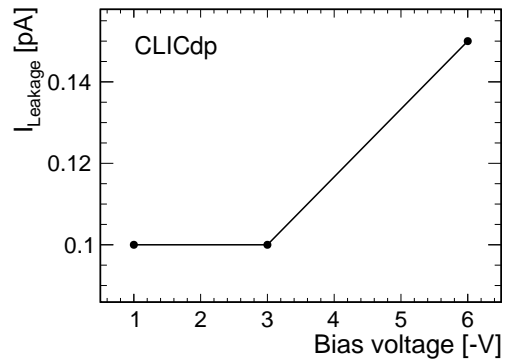Figure 17: Common mode amplitude and frequency for different bias voltages.

Figure 18: Leakage current for different bias voltages.

5.2. Noise

The mean value of the noise, averaged over all pixels of the mini-matrix, is presented in Figure 19 before and after the common mode noise correction (pixel by pixel noise fluctuations are presented in Appendix B). The noise has been reduced by a factor of $\sim 1.5 - 2$ by the common mode noise correction. Figure 19 also shows that the noise before the common mode correction is higher for higher

absolute bias voltages, while the noise after the common mode noise correction shows only a small dependance. This can be explained by the higher common mode noise amplitude for higher absolute bias voltages (see Figure 17). The noise after the common mode correction shows slightly higher values for higher absolute bias voltages, which might be attributed to the higher leakage current (see Figure 18).

In Figure 20 the mean value of the noise, averaged over all pixels of the mini-matrix, is presented before and after the common mode noise correction after applying the calibration (pixel by pixel noise fluctuations are presented in Appendix B). Higher absolute bias voltages result in lower noise in units of electrons. This is expected, since the noise in units of ADC does not strongly depend on the bias voltage and lower CF's have been measured for higher bias voltages (see Figure 13).
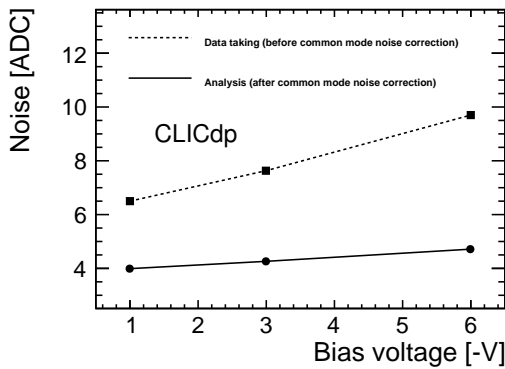

Figure 19: Noise *before the calibration*, before and after the common mode correction.
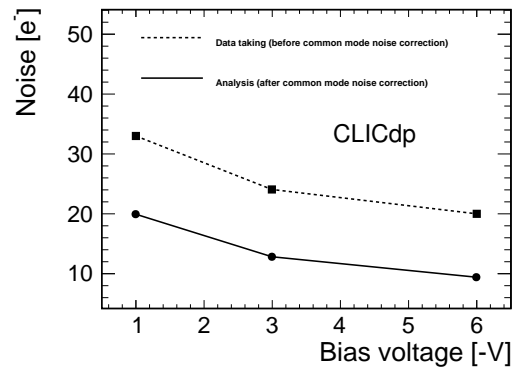
Figure 20: Noise *after the calibration*, before and after the common mode correction.

5.3. Threshold

Two different thresholds need to be distinguished. During data taking the highest pixel signal (seed signal) is required to cross a triggering threshold of

$$\text{Triggering threshold} = \text{N}_{\text{Trigger}} \times \text{Noise}_{\text{Pre common mode}}. \qquad (5)$$

During the analysis all pixels are required to cross a single pixel analysis threshold of

$$\text{Analysis threshold} = \text{N}_{\text{Single pixel}} \times \text{Noise}_{\text{Post common mode corrections}}. \qquad (6)$$

The different multiplicities are defined as $\text{N}_{\text{Trigger}}$ and $\text{N}_{\text{Single pixel}}$ and can be adjusted individually for the triggering- and the analysis threshold.

During data taking the triggering threshold has been set according to Equation (5) with a multiplicity of $\text{N}_{\text{Trigger}} = 8$. This value was set to allow for an efficient data taking where the rate of random noise triggers did not exceed a few Hz. The left plot of Figure 21 shows the triggering thresholds for different pixels before the common mode noise correction.

If not stated otherwise, the single pixel threshold during the analysis has been set according to Equation (6) with a multiplicity[5] of $\text{N}_{\text{Single pixel}} = 5$. The right plot of Figure 21 displays the analysis thresholds for different pixels before the common mode noise correction. Apart from a few outliers, the threshold values are of the same order of magnitude for all pixels given a specific bias voltage[6].

The mean values of these distributions are shown versus the bias voltage in Figure 22. Due to the higher noise, a higher effective threshold has been applied for lower bias voltages.

---

[5]The choice of $\text{N}_{\text{Single pixel}} = 5$ is justified in the threshold scan described in Section 7.2.1.

[6]According to Equation (5) and Equation (6), the outliers in the threshold values are attributed to higher noise values for a few pixels, as shown in Appendix B.
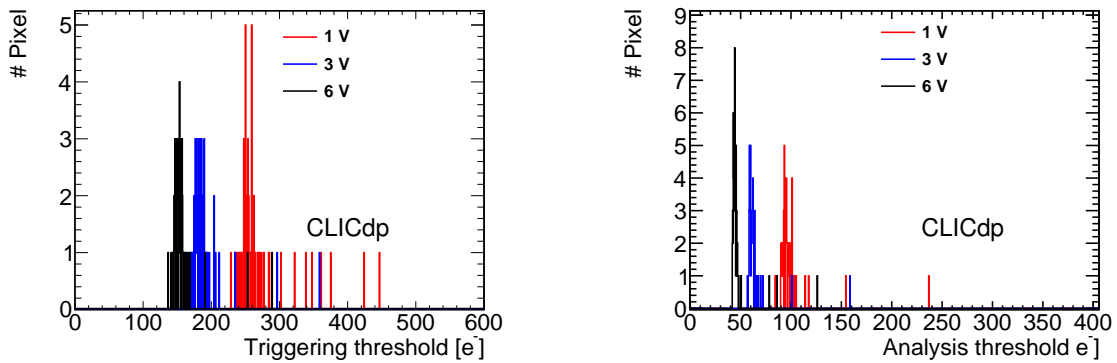
Figure 21: Triggering threshold (left plot) and analysis threshold (right plot) per pixel for different bias voltages.
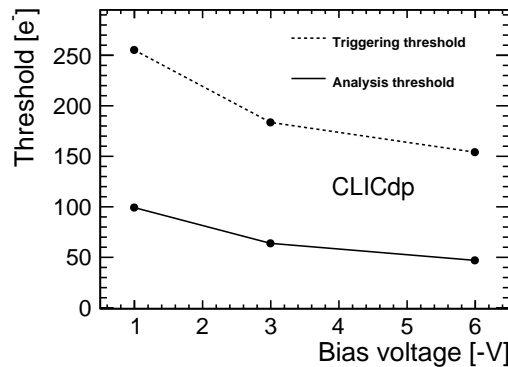

Figure 22: Triggering and analysis threshold versus bias voltage.

6. Test-beam measurements

6.1. Setup

Test-beam measurements have been performed in the H6 beam line of the CERN SPS using a beam of positively charged hadrons with an energy of 120 GeV. As a reference system for particle tracking, the CLICdp Timepix3-telescope has been used [9]. The test-beam setup is presented in Figure 23. The Investigator is placed in the centre position of six telescope planes. To optimise the tracking resolution, the telescope planes are moved as close to each other and to the Investigator, as mechanically possible. With this setup, a track spatial resolution on the Device Under Test (DUT) of $\sim 2\,\mu$m and a track timing resolution on the DUT of $\sim 1\,$ns have been achieved [9]. A Cartesian right-handed coordinate system has been selected to describe the geometry of the telescope, with the Z-direction along the beam axis as illustrated in Figure 23. The Y-direction points vertically upwards.

The Timepix3 readout ASIC [14] allows for a continuous readout with a high particle rate. The beam line parameters were set for a beam spot size of $\sim 1\,$cm^2 and a particle rate of $\sim 3\cdot10^6$ during the $\sim 5\,$s spills. Measurements were carried out for an Investigator mini-matrix with a pixel size of $28 \times 28\,\mu$m^2, resulting in an active area of $0.224 \times 0.224\,$mm^2. The small active area, as well as dead times of the Investigator during the reset pulse and the data readout (see Section 2.3) result in an Investigator trigger rate in the order of a few hundred Hz during the $\sim 5\,$s spills.
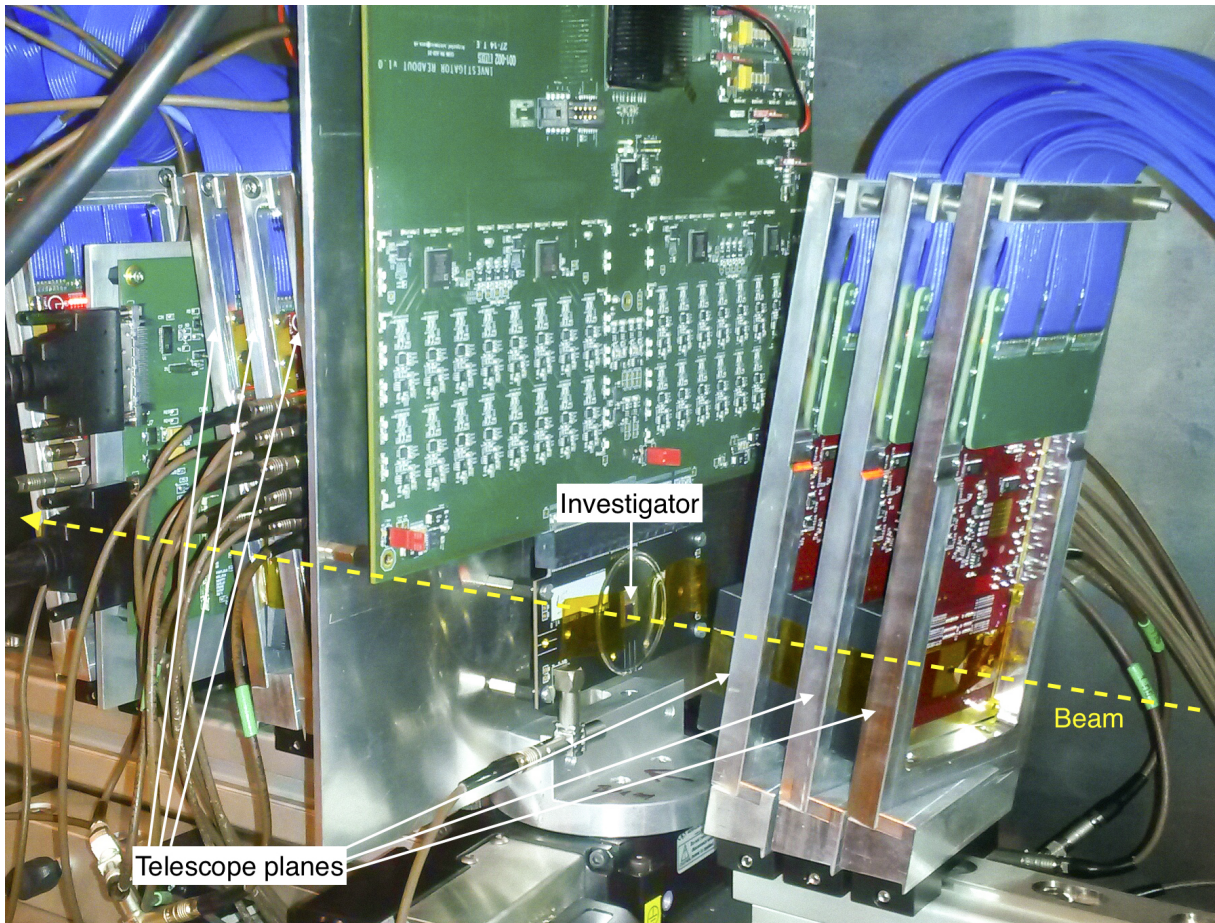
Figure 23: Test-beam setup of the CLICdp Timepix3-telescope in the H6 beam line of the CERN SPS.

6.2. Trigger logic

The chips of the telescope planes are masked during the dead times of the Investigator. To achieve this, the INVROS creates a veto signal during all times in which the Investigator chip or the readout are inactive. This happens periodically during the recovery time after the reset pulse (see Section 2.3 and Figure 3) for about 13 µs, and for a few ms after a particle hit has been detected during the readout phase. Additionally, to be able to precisely determine the phase of tracks and hits within the Investigator cycle, the falling edge of the veto signal, which corresponds to the release of the telescope veto, is time tagged using one of the Time to Digital (TDC) inputs of the telescope readout system. For that, a pulse generator has been used to convert the falling edge into a short pulse. The long veto after a particle hit, needed to complete the readout of the samples in the active window, could not reliably be generated by the INVROS firmware: the longer veto after a particle hit was released too early, and the telescope started taking data before the INVROS could follow. To still be able to perform a proper efficiency measurement, the veto signal has been extended using a Nuclear Instrument Module (NIM) gate generator, as shown in Figures 24 and 25.

The gate generator is started by the trigger pulse, the gate reset is triggered by the readout software and sent via an Arduino Uno micro controller board to the gate reset input. The reset signal is issued as close as possible to the end of the inactive period during the readout cycle, directly before the readout software is ready to acquire the next event. Note that the Investigator clock and the telescope clock are not synchronised during data taking. To be able to synchronise the Investigator time stamps with the telescope reference clock offline, a trigger signal is sent from the INVROS to one of the telescope TDC
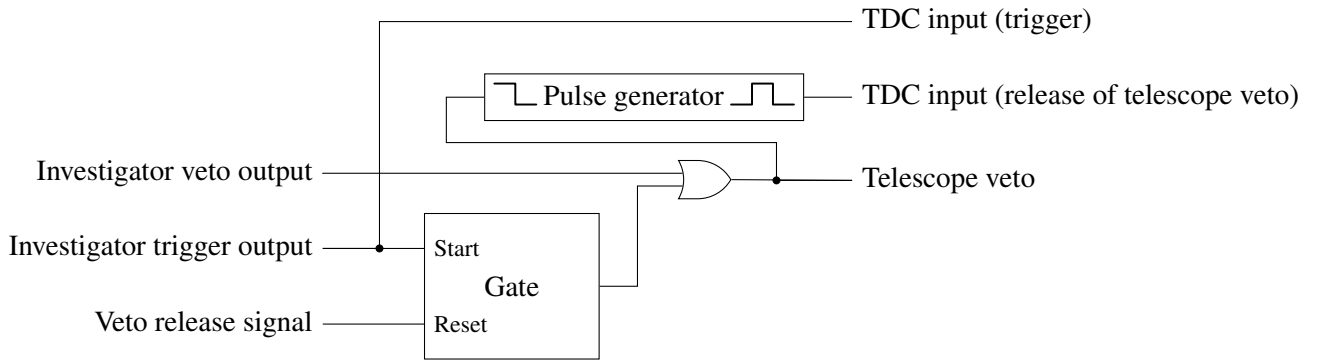
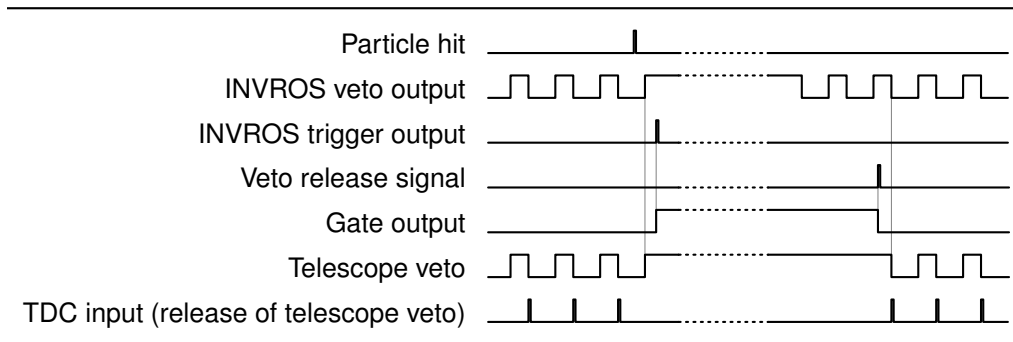Figure 24: Schematic of the veto and trigger logic.

Figure 25: Timing diagram illustrating the extension of the veto signal after a particle hit.

inputs if a particle hit has been detected. This trigger signal is sent with a constant delay after the end of the active Investigator window (see Figure 3) and then stored in the telescope data file with a time stamp from the telescope reference clock.

6.3. Offline synchronisation of Investigator and Timepix3-telescope data

Since no synchronised clock has been used for the Investigator and the Timepix3-telescope data taking, the synchronisation has been performed by an offline procedure during the event building. This procedure is illustrated in Figure 26 and described in the following text. It should be noted that the Timepix3 hit data are not send out from the chip in strict time order; due to the data driven readout [14].

During the event building, 100 ms of the recorded raw data are read out from the event files and filled into a vector. The recorded raw data includes the single pixel time stamps from the telescope planes as well as the time stamps of the release of the telescope veto and the Investigator trigger time stamps. This is illustrated in Step 1 of Figure 26, where the different numbers correspond to different time stamps in arbitrary units.

To calculate the absolute Investigator hit time with respect to the Timepix3 reference clock, the nth Investigator trigger time stamp is assigned to the nth Investigator event (see Step 2 in Figure 26). A constant time delay has been observed between the Investigator trigger time stamps and the telescope hit time stamps, which can be attributed to two different effects: the length of the cables bringing the Investigator trigger signal from the Investigator readout system to the Telescope readout system, and the fixed time delay after the Investigator readout, at which the trigger signal is sent from the INVROS to the telescope planes. The offset is calculated in a later stage of the analysis (by comparing the time stamp of a track through the Investigator to the time stamp of the matched trigger) and has been found to be in the

order of a few hundred ns. The time stamp assigned to the nth Investigator event is then calculated as

$$t_{Investigator\ event\ n} = t_{trigger\ n} - offset. \tag{7}$$

The difference Δ between the single pixel hit time t_{hit} (which can be at an arbitrary time within the readout window) and the end of the readout window is subtracted from this time stamp to obtain the absolute time stamp $t_{hit\ absolute}$ of a hit in an Investigator pixel

$$t_{hit\ absolute} = t_{Investigator\ event\ n} - \Delta. \tag{8}$$

The reconstructed absolute single pixel Investigator time stamps $t_{hit\ absolute}$ are further inserted in the 100 ms vector, which already contains the time stamps of the telescope hits (see Step 3 of Figure 26).

Next, the time stamps in the 100 ms vector are ordered descending in time (see Step 4 in Figure 26). Starting from the earliest time stamp, the time stamps in the 100 ms vector are separated into smaller units of 10 µs duration and removed from the 100 ms vector (see Step 5 in Figure 26). Each 10 µs unit is defined as an event in the following analysis. Before the 100 ms vector is empty, it gets refilled with new data (see Step 6 in Figure 26) and the procedure repeats iteratively from Step 2 in Figure 26, until all data have been read out. By refilling the 100 ms vector before it is empty and building the 10 µs events from this vector, an assignment of hits into the wrong event, due to effects in the transition region between two 100 ms data chunks, can be avoided.

6.4. Event reconstruction and quality cuts

6.4.1. Clustering and position reconstruction

A clustering of the pixels in an event is performed using the processor `EUTelClusteringProcessor` of the EUTelescope framework [15]. The position of the cluster is obtained by charge interpolation between the pixels. An η-correction has been used in addition, to correct for non linear charge sharing effects. For the η-correction the EUTelescope processor `EUTelCalculateEtaProcessor` has been used, which calculates the η-correction in a data driven way (as described in [16]) during the analysis.

6.4.2. Alignment

The telescope alignment has been performed with the processor `EUTelMille` of the EUTelescope framework [15].

This processor makes use of the Millepede algorithm [17] to perform a minimisation of the track residuals, where the track residual is defined as the difference in space between the reconstructed hit position on the telescope plane and the predicted track position on this plane. To align the Investigator with respect to the telescope reference system, the Investigator residual, defined as the difference between the reconstructed Investigator hit position and the interpolated track position on the Investigator, is calculated. The Investigator is then aligned with respect to the telescope reference system by shifting the Investigator position until the remaining offset in X- and Y-direction between the track and hit is zero. To reduce the impact of movements of the Investigator chip over a longer time scale the alignment is performed for each a few minutes long run separately. This short run time results in too low statistics to be sensitive to the rotations of the small chip within the telescope. For this reason tilts of the Investigator with respect to the telescope reference system are not corrected [7].

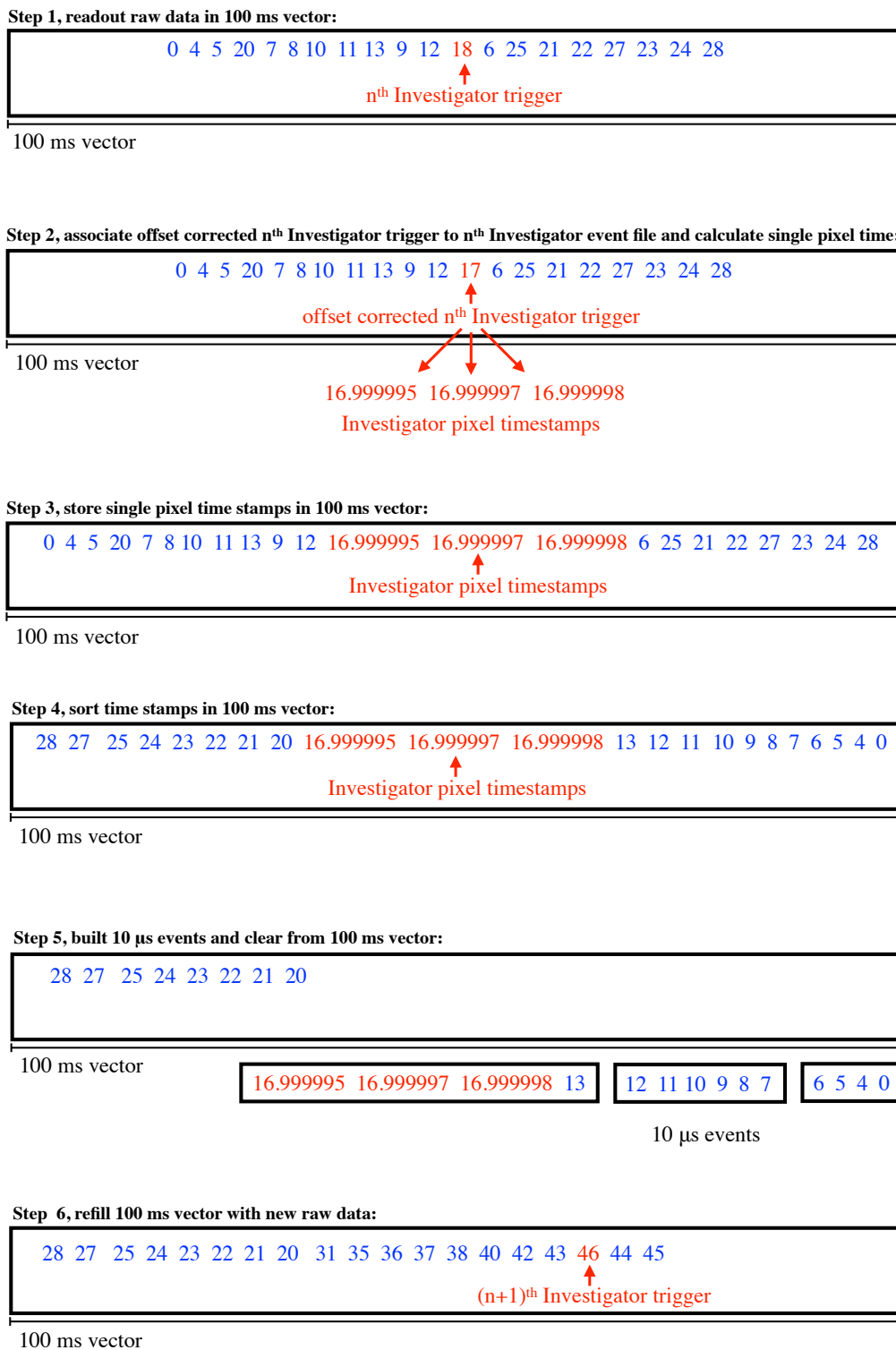[7]The reconstruction assumes, that the Investigator is placed perfectly parallel to the XY-plane of the telescope reference system.

Step 1, readout raw data in 100 ms vector:

0 4 5 20 7 8 10 11 13 9 12 18 6 25 21 22 27 23 24 28

nth Investigator trigger

100 ms vector

Step 2, associate offset corrected nth Investigator trigger to nth Investigator event file and calculate single pixel time:

0 4 5 20 7 8 10 11 13 9 12 17 6 25 21 22 27 23 24 28

offset corrected nth Investigator trigger

100 ms vector

16.999995 16.999997 16.999998
Investigator pixel timestamps

Step 3, store single pixel time stamps in 100 ms vector:

0 4 5 20 7 8 10 11 13 9 12 16.999995 16.999997 16.999998 6 25 21 22 27 23 24 28

Investigator pixel timestamps

100 ms vector

Step 4, sort time stamps in 100 ms vector:

28 27 25 24 23 22 21 20 16.999995 16.999997 16.999998 13 12 11 10 9 8 7 6 5 4 0

Investigator pixel timestamps

100 ms vector

Step 5, built 10 µs events and clear from 100 ms vector:

28 27 25 24 23 22 21 20

100 ms vector

| 16.999995 16.999997 16.999998 13 | 12 11 10 9 8 7 | 6 5 4 0 |

10 µs events

Step 6, refill 100 ms vector with new raw data:

28 27 25 24 23 22 21 20 31 35 36 37 38 40 42 43 46 44 45

(n+1)th Investigator trigger

100 ms vector

Figure 26: Flowchart of the steps for the offline synchronisation of the Investigator and Timepix3-telescope data. The integer numbers symbolise telescope time stamps in arbitrary units. The floating point numbers symbolise Investigator pixel time stamps.

6.4.3. Track quality and track matching

A reconstructed telescope track is required to have maximally one missing hit in the telescope planes and to have a $\chi^2/\text{ndof} < 100$. After aligning the Investigator with the telescope planes, a reconstructed Investigator hit is matched to a reconstructed telescope track, if their spatial distance is smaller than $100\,\mu\text{m}$. Moreover, the Investigator hit and telescope track need to be within the $10\,\mu\text{s}$ time window of one event, to be matched together.

6.4.4. Edge masking

Tracks passing through the outer half of the edge pixels are discarded to avoid a bias of charge sharing observables due to missing neighbouring pixels and to avoid effects from the track prediction resolution.

6.4.5. Timing cuts

Further cuts are performed on the time stamp of the reconstructed tracks with respect to the phase within the investigator readout cycle (see Figure 24 and 25). The discriminator outputs from the pixels of the telescope planes and the telescope veto release signal are connected in an and-gate. Since the discriminator output pulse length (Time over Threshold ToT) is proportional to the signal amplitude, it is not infinitely short. For this reason three different cases, shown in Figure 27 need to be distinguished:

Case 1 If the telescope veto (from the gate output in Figure 24) is released before the discriminator output of the telescope hit crosses the threshold, the stored telescope hit time stamp is set correctly to the the time where the telescope signal pulse crosses the threshold.

Case 2 If the telescope veto is released after the discriminator output of the telescope hit has dropped below threshold, no telescope hit is read out. This is intended, since the Investigator can not record the hit in the dead time before the telescope veto is released.

Case 3 In the last case, Case 3, the telescope veto is released while the discriminator output of the telescope hit is above threshold. In this case a telescope hit is read out and the telescope hit time stamp is set wrongly to the time stamp of the telescope veto release.
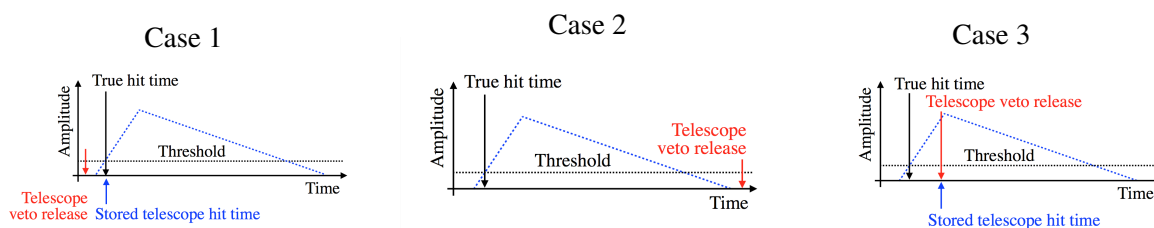
Figure 27: Different cases of telescope release time with respect the time of a particle hit in the telescope.

In Figure 28 the difference between the track time stamp and time stamp of the telescope veto release is presented. Tracks from Case 3 in Figure 27, result in tracks with a wrong time stamp of the telescope veto release and therefore peak at zero in Figure 28. Since the corresponding particle has not been recorded by the Investigator, these wrongly reconstructed tracks have no matched Investigator hit and can not be used for efficiency measurements. For that reason, tracks in the first $1\,\mu\text{s}$ after the telescope veto is released are excluded from the analysis.

A second peak at zero can be observed in Figure 28, which is due to tracks matched to an Investigator hit. This is expected, as the telescope active window is shifted to later times with respect to the active Investigator window. Figure 29 shows an illustration of the shift of the grey Investigator active window
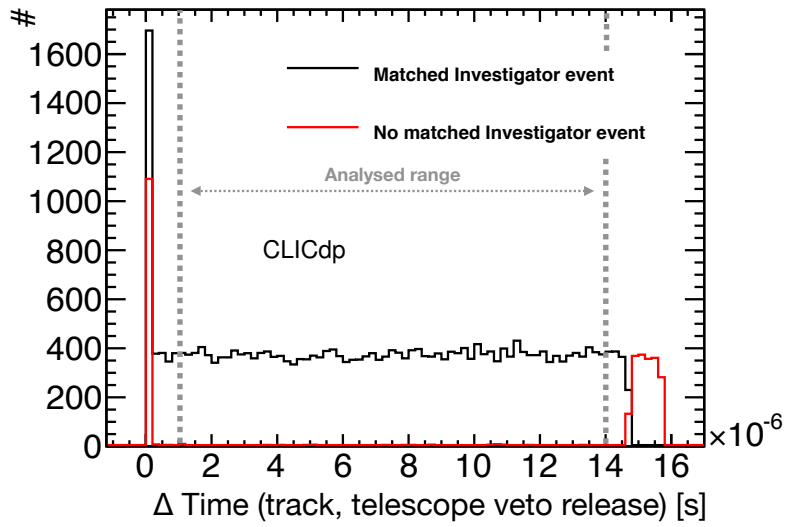
Figure 28: Histogram of the difference between the track time stamp and time stamp of the telescope veto release. All tracks outside a range of $[1\,\mu\mathrm{s}, 14\,\mu\mathrm{s}]$ are masked, as discussed in the text.

with respect to the red telescope active window. This shift is expected due to delays from cables and veto signal generation (as discussed in Section 6.3). As a consequence of this shift, a time region of a few 100 ns is created, in which the signal pulse can cross the threshold before the telescope veto has been released.
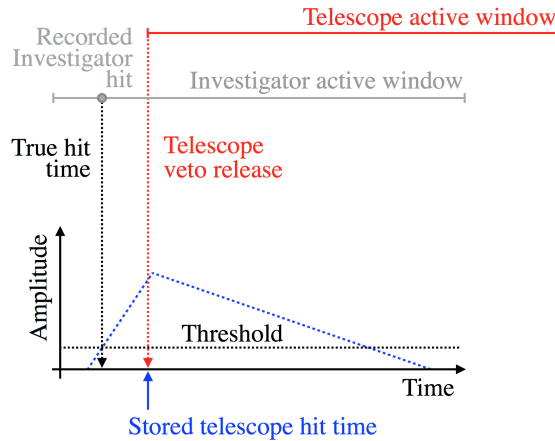
Figure 29: Explanation of peak of matched tracks at a zero value in Figure 28.

This results in the contribution of tracks matched to an Investigator hit in the zero peak of Figure 28. Note that these tracks are filtered out by the requirement that tracks in the first $1\,\mu\mathrm{s}$ after the telescope is released are excluded from the analysis. The Investigator active window being shifted to earlier times with respect to the telescope active window also results in non-matched tracks at the end of the histogram in Figure 28. To filter out these artefacts of the not perfectly aligned Investigator active and telescope active windows, tracks after $14\,\mu\mathrm{s}$ after the shutter is opened are excluded from the analysis.

7. **Test-beam results**

7.1. **Results for nominal operation conditions**

A bias voltage of $-6\,\mathrm{V}$, a triggering threshold of $\sim 150\,\mathrm{e}^-$ and an analysis threshold of $\sim 50\,\mathrm{e}^-$ have been applied at nominal operation conditions.

7.1.1. **Cluster size and spatial resolution**

The total cluster size distribution is presented in Figure 30. The distribution has a mean value of ~ 1.9 and shows that in $\sim 55\,\%$ of the clusters, the charge is shared between the pixels. The small peak at a cluster size of four can be understood by the square pixel shape. To illustrate this, the total cluster size is represented in the following way: A two-dimensional histogram with the dimensions of a single-pixel cell is filled at each track intercept position within the hit pixel. Using this representation, all tracks are mapped into a single-pixel cell (in-pixel representation). Figure 31 displays the in-pixel representation of the total cluster size.
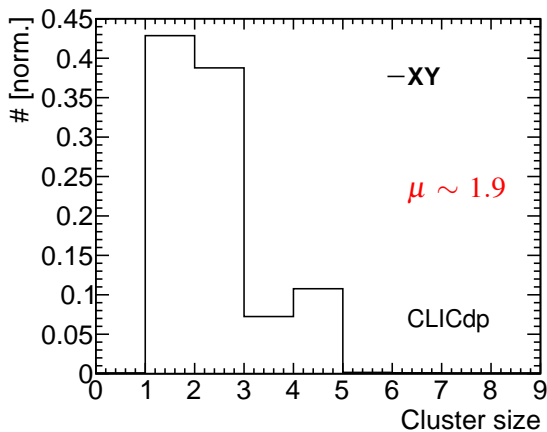
Figure 30: Total cluster size distribution.
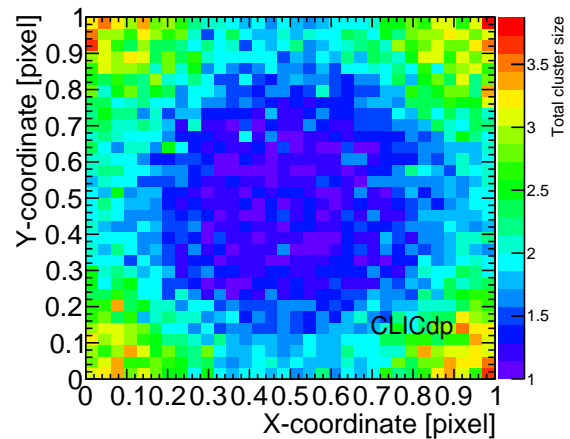
Figure 31: Total cluster size at the track intercept position within the pixel cell.

As expected from the discussion in Section 2.2, more single-pixel clusters are observed for a track intercept position close to the pixel centre. Close to the pixel edges a cluster size of two is the most prominent. Due to the square shape of the pixel, the distance to three neighbouring pixels gets minimised in the pixel corners and a cluster size of four dominates that region. A cluster size of three can be observed in the geometrically slightly smaller regions further away from the pixel corners. For this reason slightly more clusters with a cluster size of four compared to a cluster size of three can be observed in Figure 30.

In Figure 32 the cluster size only in one direction of the Investigator mini-matrix (X or Y) is presented, showing that, in $\sim 40\,\%$ of the clusters, the charge is shared between two pixels in one direction of the mini-matrix. For the two pixel clusters in X- and Y direction, a charge interpolation can be performed between the pixels and the position resolution is expected to be improved. The spatial residuals between the reconstructed Investigator hit position and the telescope track intercepts are shown in Figure 33 for the X- and Y-direction.

A spatial resolution of $\sim 6\,\mu\mathrm{m}$ is obtained in X- and Y-direction of the mini-matrix, the resolution defined as the Root Mean Square (RMS) of the distributions on a range of $\pm 20\,\mu\mathrm{m}$. This can be compared to the value of $\mathrm{Width}/\sqrt{12} = \mathrm{pitch}/\sqrt{12} \sim 8\,\mu\mathrm{m}$, which would be expected if there were only single-pixel clusters.
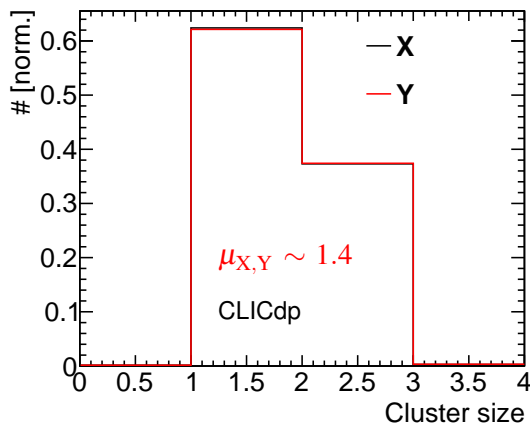
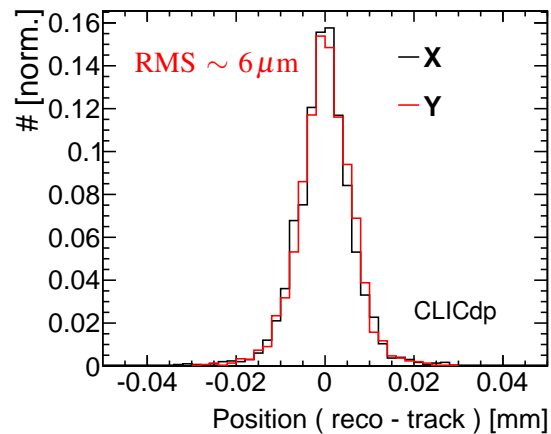Figure 32: Cluster size in X- and Y-direction of the pixel matrix.

Figure 33: Spatial X- and Y-residual distributions.

The residual in X- and Y-direction are displayed separately for single-pixel clusters and multi-pixel clusters in Figure 34.
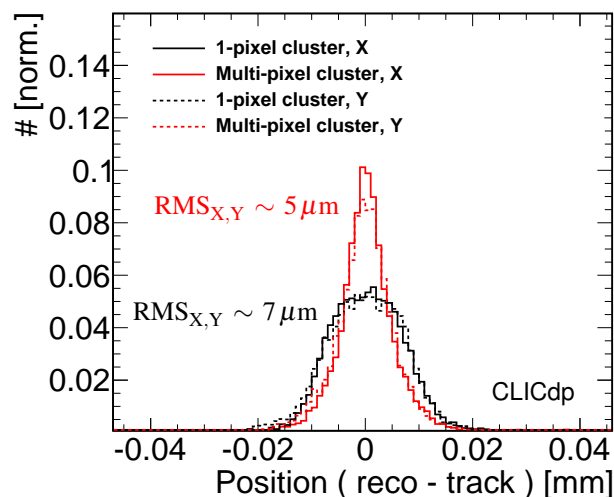

Figure 34: Spatial X- and Y-residual distribution, separately for single- and multi-pixel clusters.

A RMS of $\sim 5\,\mu$m has been calculated for multi-pixel clusters, being improved with respect to the RMS of $\sim 7\,\mu$m for single-pixel clusters. Also the RMS for single-pixel clusters is improved with respect to the value of pitch/$\sqrt{12}$. This can be explained by the fact that the area in which single pixel clusters are generated is smaller than the full pixel area, so that the Width in the formula Width/$\sqrt{12}$ is not the pixel pitch but effectively smaller. The effect can be observed in the in-pixel representation of the cluster size in X- and Y-direction (Figure 35 and 36).

Overall, the obtained results show that the analogue performance of the studied Investigator mini-matrix with a pixel size of $28\,\mu$m reaches the requirement of a single point resolution of $7\,\mu$m for the CLIC tracker.
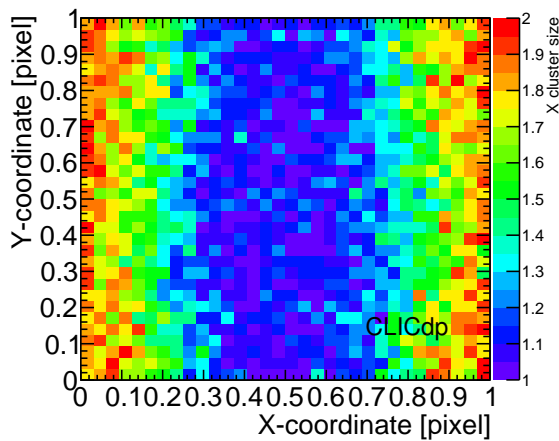
Figure 35: X cluster size at the track intercept position within the pixel cell.
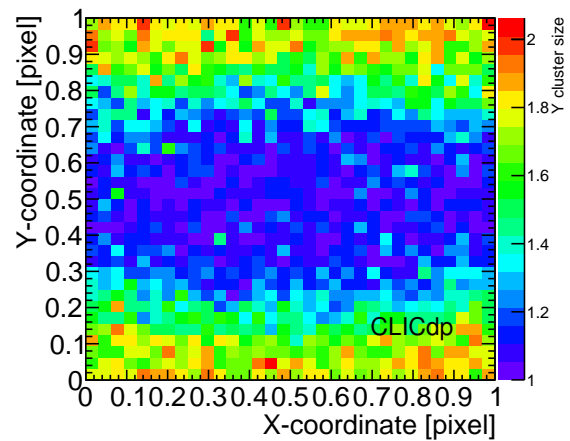
Figure 36: Y cluster size at the track intercept position within the pixel cell.

7.1.2. Timing resolution

The timing residual is defined as the distance in time between the reconstructed Investigator hit and the associated track. The time of the reconstructed Investigator hit is defined as the hit time (see Chapter 3) of the first pixel. A timing resolution of $\sim 5\,\text{ns}$ is obtained when calculating the RMS of the timing residual distribution shown in Figure 37, on a range of $\pm 0.05\,\mu\text{s}$.
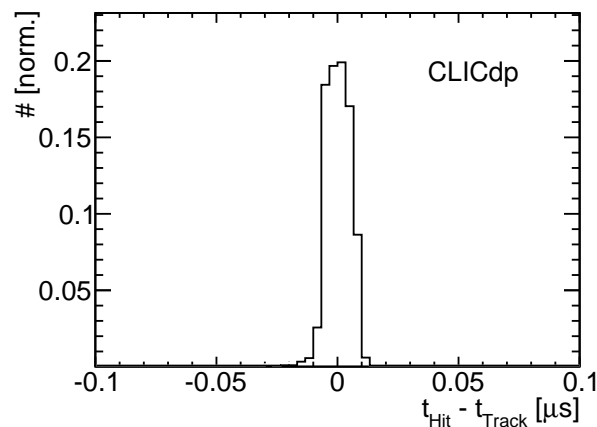
Figure 37: Distribution of the timing residual, defined as the difference in time between a reconstructed telescope track and the first pixel in the matched Investigator hit.

The measured timing resolution is probably limited by the used setup, e.g. the sampling frequency of 65 MHz of the ADCs as well as the $\sim 10\,\text{ns}$ rise time of the output buffers in the Investigator periphery[8].

---

[8]As shown in Section 7.2.2 the measured timing resolution does not depend on the bias voltage, hinting at the fact that it is not dominated by the sensor but by the used setup.

7.1.3. Signal and efficiency

The distribution of the highest signal in a cluster (seed signal) is presented in Figure 47, showing a Most Probable Value (MPV) at $\sim 1.5 \mathrm{ke}^-$. To study the effect of charge sharing on the seed signal, the mean seed signal is shown in an in-pixel representation in Figure 39. By comparing Figure 31 and Figure 39 it is clear that an increased amount of charge sharing between pixels is correlated with a lower mean seed signal.
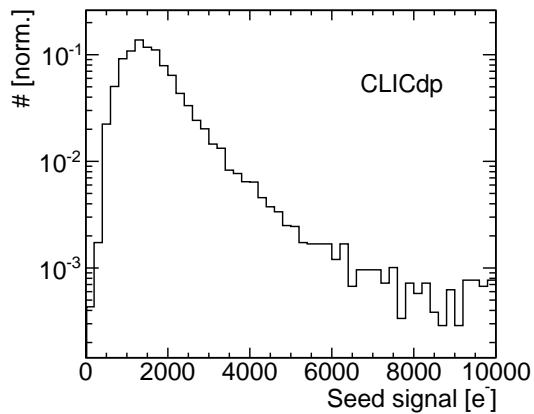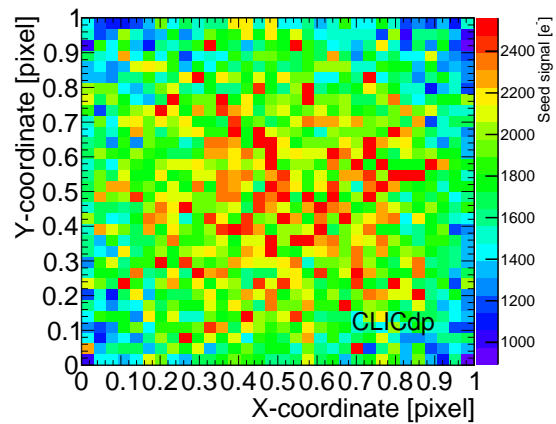

Figure 38: Seed signal distribution.

Figure 39: Mean seed signal within the pixel cell.

The lower seed signal in the pixel corners can result in a lower efficiency if the seed signal drops below the triggering threshold during data taking. To study this, the detection efficiency is calculated as the number of tracks passing through the fiducial region on the Investigator mini-matrix with a matched Investigator hit, divided by the total number of tracks reconstructed through the fiducial region on the Investigator mini-matrix[9]. The detection efficiency is shown in an in-pixel representation in Figure 40.
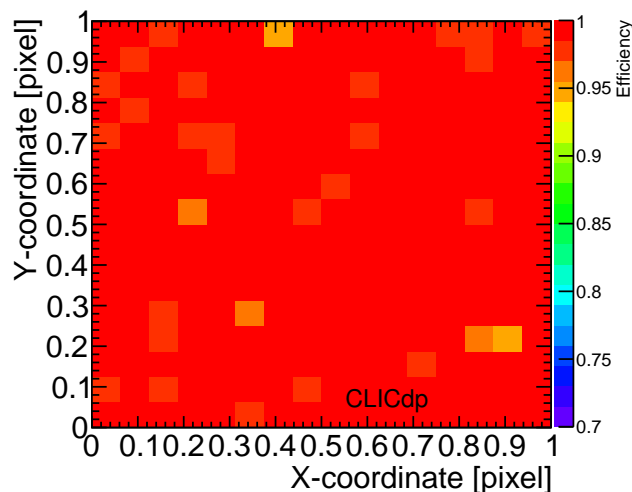
Figure 40: Efficiency within the pixel cell. Each bin contains ~ 90 tracks.

---

[9]As discussed in Section 6.4.4, the fiducial region on the Investigator mini-matrix is defined after cutting out the outer half of the edge pixels.

A homogenous and overall high efficiency can be observed within the pixel cell, showing that the charge sharing does not affect the particle detection capability of the studied Investigator mini-matrix.

The efficiency across the pixel matrix is presented in Figure 41 in the Investigator reference frame, showing a uniform and overall high efficiency across the pixel matrix. The size of each pixel of 28×28 μm^2 is indicated by the squares surrounded by the black dashed grid. An average efficiency of 99.26 % was calculated in the fiducial region on the Investigator mini-matrix, shown inside the white line in Figure 41.
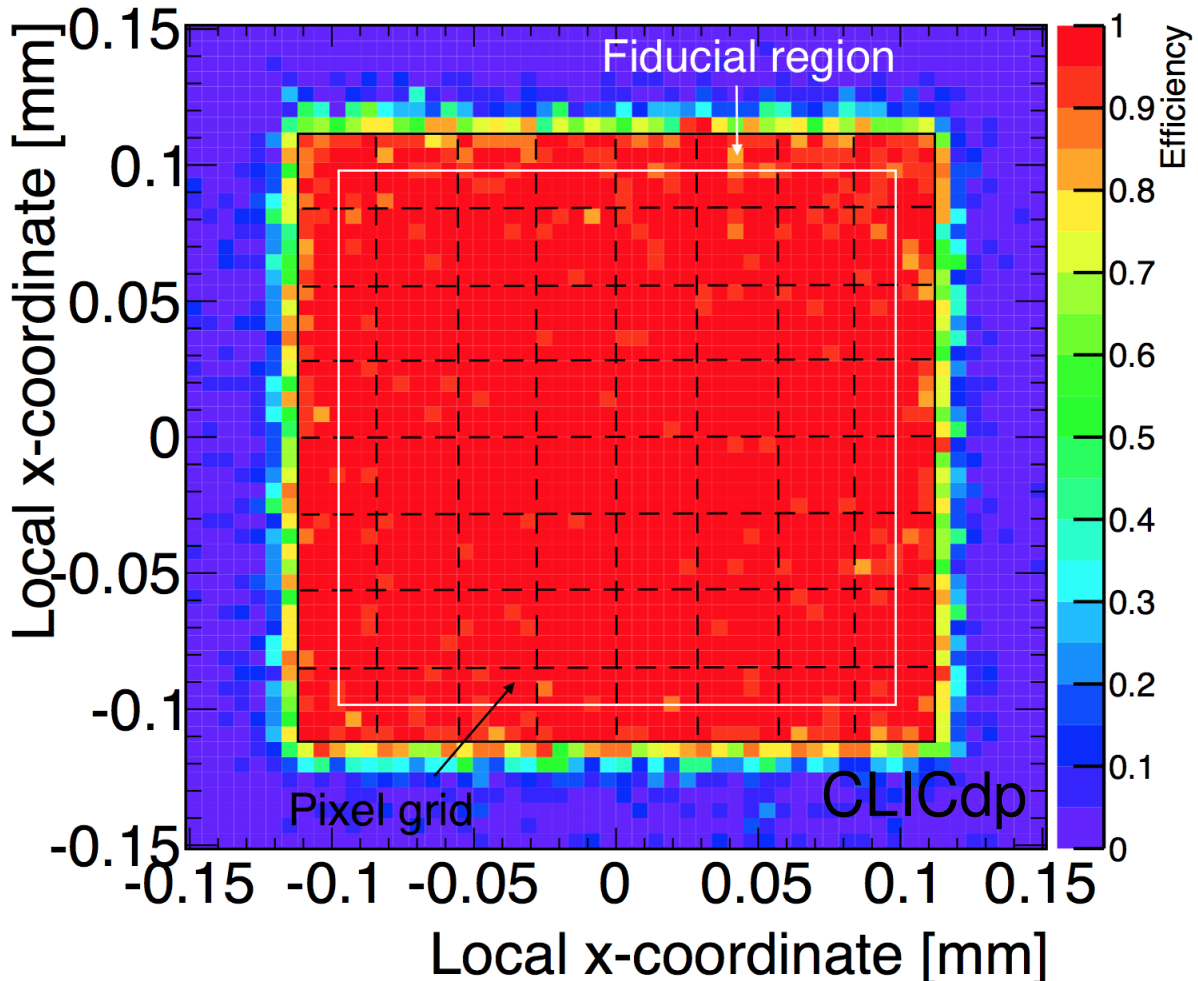
Figure 41: Efficiency across the pixel matrix in the Investigator reference frame.

The statistical uncertainty has been calculated as the uncertainty on the mean value for a counting experiment with two possible outcomes. The two possible outcomes are an efficiency entry of 1 if the track is matched to an Investigator hit, or an efficiency entry of 0 if the track is not matched to an Investigator hit. This results in an uncertainty of $\sigma_{stat.} = \sqrt{p \cdot (100 - p)/N} \, [\%]$, with the number of experiments N and the probability p for a positive outcome of the experiment in percent. The number of experiments is interpreted as the number of N = 21052 tracks recorded through the fiducial region. The best guess for the probability p of a positive outcome is the measured average efficiency.
This gives a statistical uncertainty of

$$\sigma_{stat.,Efficiency} = \sqrt{99.26 \cdot (100 - 99.26)/21052} \, \% = 0.06 \, \%. \tag{9}$$

To investigate the origin of the efficiency loss of 0.74 %, the tracks that pass through the fiducial region

and have not been matched to an Investigator hit (non-matched tracks) are studied. The time stamp of these tracks is plotted with respect to the following Investigator trigger in time, in Figure 42.
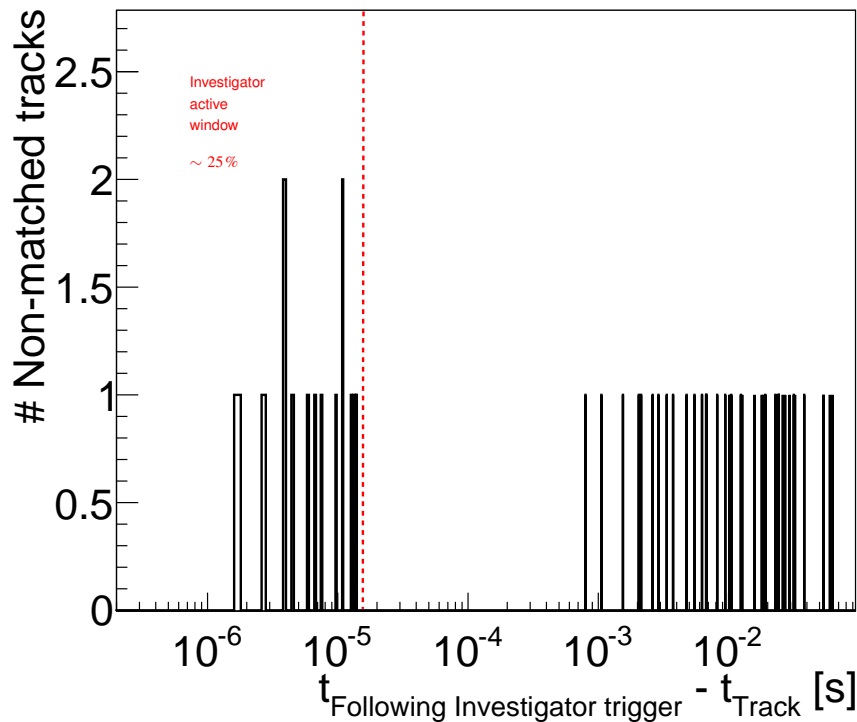

Figure 42: Difference in time between the non-matched tracks and the next Investigator trigger in time.

If the track that goes through the fiducial region has triggered the Investigator, an Investigator trigger is found in the first $15.75\,\mu$s of Figure 42, corresponding to the size of the active Investigator window. In all of these cases, an Investigator event has been read out but not reconstructed by the analysis. These events are not reconstructed by the analysis because they show e.g. a spatial distance larger than the $100\,\mu$m of the track matching cut. This is expected from multiple scattering of the particles in the telescope. Tracks from multiple scattering with a bad $\chi^2/$ndof are not excluded in the analysis due to the loose cut on the $\chi^2/$ndof of the telescope tracks (see Section 6.4.2).
Approximately 25 % of the non-matched tracks fall into this category, corresponding to $0.25 \cdot 0.74\,\%$ $\sim 0.2\,\%$ of the measured in-efficiency. To show that these cases are originating from badly reconstructed tracks, the analysis has been redone with the requirement on the telescope tracks of $\chi^2/$ndof < 5, recovering $\sim 0.20\%$ of the efficiency. Thus, a systematic uncertainty has been estimated to be $\sim 0.2\%$:

$$\text{Efficiency} = (99.26 \pm 0.06\,\text{stat.} \pm 0.20\,\text{syst.})\,\%. \tag{10}$$

Half a percent of the in-efficiency originates from tracks with no associated trigger (see entries outside the Investigator active window in Figure 42).

7.2. Results for parameter scans

7.2.1. Threshold scan

As discussed before, the triggering threshold has been optimised, so that the rate of random noise triggers did not exceed a few Hz (see Chapter 5). To optimise the analysis threshold applied offline, a scan of this threshold has been performed. For the interplay of both threshold values, two different cases need to be distinguished:

1. Analysis threshold below triggering threshold:
   The triggering threshold requires at least one pixel to be above the given value, and can be therefore considered as the threshold on the seed signal. The analysis threshold has been applied to each single-pixel, and therefore defines the threshold on the signal of the neighbouring pixels. Since only the neighbouring pixels can be affected, the efficiency is expected to be unaffected while the cluster size and the resolution are expected to change.

2. Analysis threshold at least as high as triggering threshold:
   As soon as the analysis threshold crosses the triggering threshold, the value of the analysis threshold defines a global threshold value, being the same for all pixels. Since in this range of varying the analysis threshold the neighbouring pixels as well as the seed pixel are affected, also the efficiency is expected to be affected.

Results are presented for a bias voltage of $-6\,\text{V}$. The cluster size distributions in the X-direction are presented for different analysis thresholds in Figure 43 and the mean values of the distributions as well as their statistical uncertainties are shown in Figure 44. As expected, the cluster size is reduced for higher analysis thresholds, since the signal of neighbouring pixels falls below the analysis threshold.
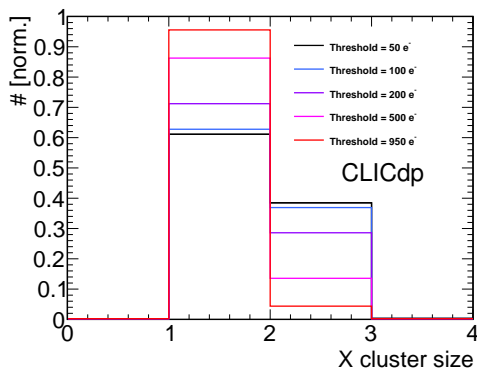
Figure 43: Custer size distributions in X-direction for different analysis thresholds.
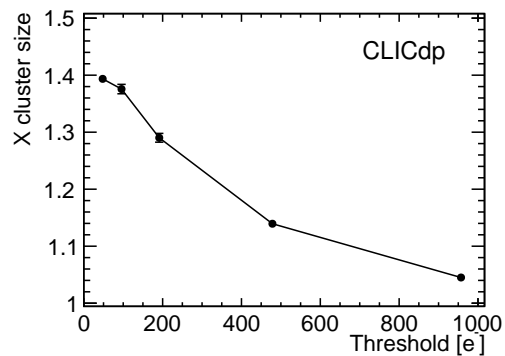
Figure 44: Mean cluster size in X-direction versus analysis threshold.

This trend is reflected in a degradation of the spatial resolution and can be observed in the spatial X-residual distributions shown for different analysis thresholds in Figure 45. The X-resolution is defined as the RMS of the spatial X-residual distribution on a range of $\pm 30\,\mu$m. In Figure 46, the X-resolution and its statistical uncertainties are presented versus the analysis threshold. At a threshold of $> 500\,\text{e}^-$, a mean cluster size close to one can be observed, showing, that almost all clusters are single-pixel clusters. As a consequence, the resolution converges to a value of $\text{pitch}/\sqrt{12} \sim 8\,\mu$m.

The efficiency with its statistical uncertainty is shown for different analysis thresholds in Figure 48. At high values of the analysis threshold of $> 500\,\text{e}^-$ the efficiency shows a strong degradation. At such high values the analysis threshold starts to significantly cut into the distribution of the seed signal (see Figure 47).

Following the discussion above, a seed threshold of $< 500\,\text{e}^-$ is necessary to obtain a fully efficient operation of the studied mini-matrix. To achieve an optimal spatial resolution by maximising the cluster size, an analysis threshold as low as possible is needed. Further, to sufficiently suppress the noise, the lowest value of the analysis threshold has been set to be five times higher than the noise.
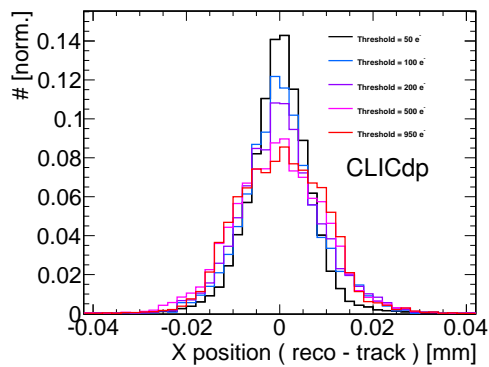
Figure 45: Spatial residual distributions in X-direction for different analysis thresholds.
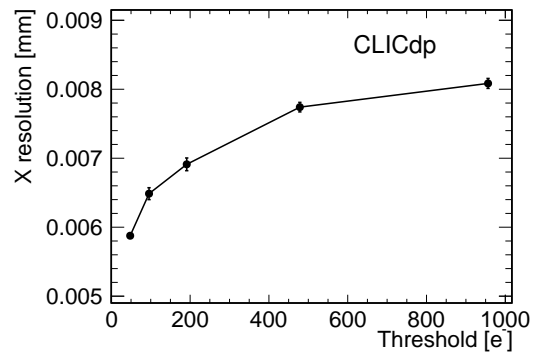

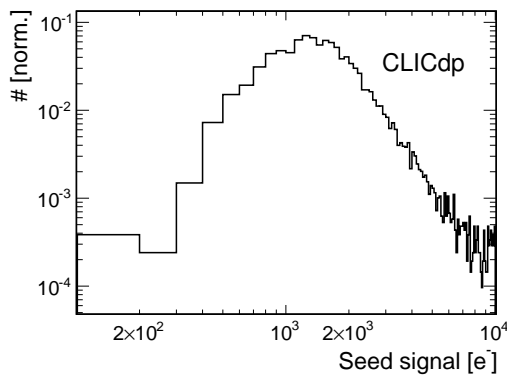Figure 46: Resolution in X-direction versus analysis threshold.

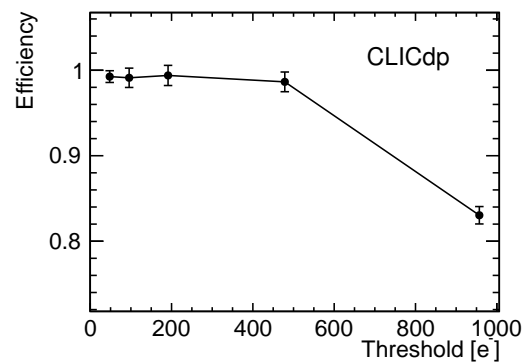Figure 47: Seed signal for a low analysis threshold of $\sim 50\,e^-$.

Figure 48: Efficiency versus analysis threshold.

7.2.2. Bias voltage scan

A bias voltage scan has been performed to investigate the optimal operation bias voltage. The chip has been operated at three different bias voltages, $-6\,V$, $-3\,V$ and $-1\,V$.

As discussed previously, the threshold values have been set for different bias voltages to a fixed value of threshold/noise, resulting in a lower threshold in units of electrons for higher absolute bias voltages (see Chapter 5). Accordingly, the cluster size increases for higher absolute voltages, resulting in a slight improvement of the resolution. This is visible in Figure 49 and 50, where the cluster size and the residual distributions in X-direction are presented for different bias voltages. The distributions show that the effect is not very strong. However, the mean cluster size versus bias voltage as well as the resolution, defined as the RMS of the residual distribution on a range of $\pm 20\,\mu m$, show the expected trend of slightly lower cluster sizes and worse resolution for lower absolute bias voltages. This can be observed in Figure 51 and 52, where the mean X-cluster size and the X-resolution with their statistical uncertainty are presented.

The change in threshold for different bias voltages does not significantly affect the efficiency, as visible in Figure 53. This can be explained by the fact that the seed signal distribution does not change significantly for different bias voltages (see in Figure 54). The highest threshold of $\sim 250\,e^-$ has been applied for a bias voltage of $-1\,V$. This is consistent with the results of the threshold scan, where a significant efficiency loss has been observed only above $500\,e^-$.
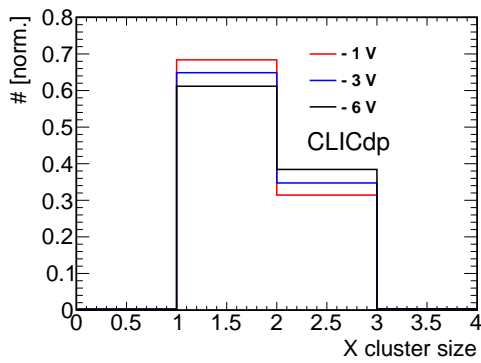
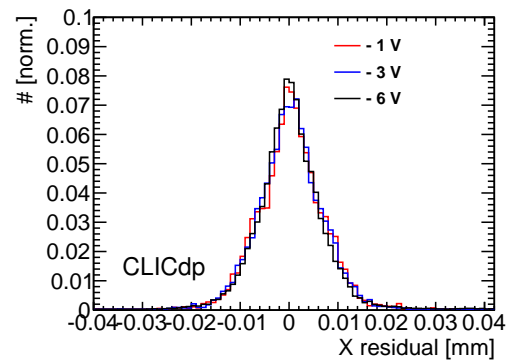Figure 49: Custer size distribution in X-direction for different bias voltages.

Figure 50: Spatial residual distribution in X-direction for different bias voltages.
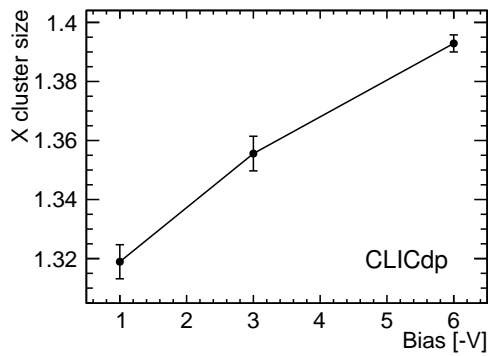

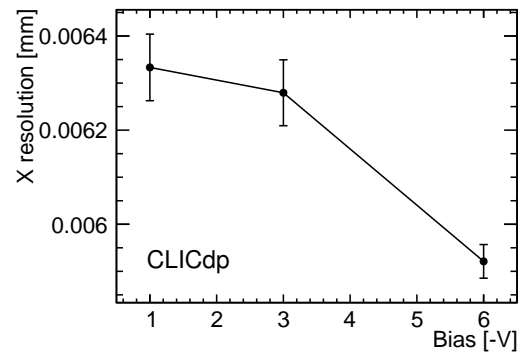Figure 51: Mean cluster size in X-direction versus bias voltage.

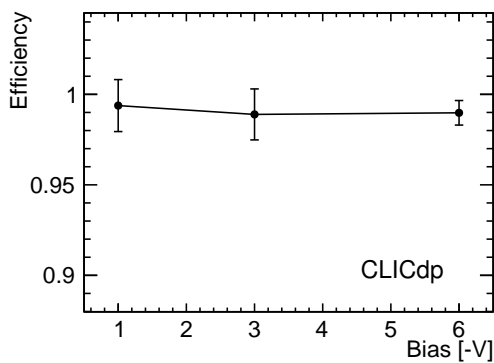Figure 52: Resolution in X-direction versus bias voltage.

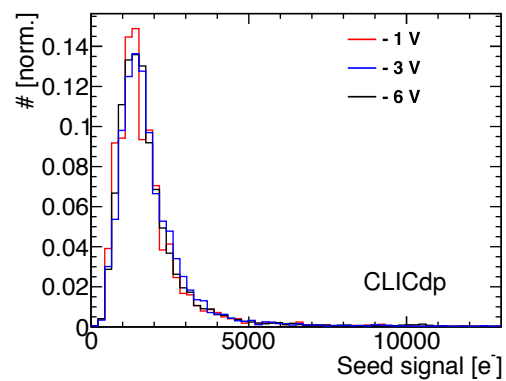Figure 53: Efficiency versus bias voltage.

Figure 54: Seed signal for different bias voltages.

Different bias voltages are expected to change the depleted region and the electric field in the sensor. To study if lower absolute bias voltages therefore result in a degradation of the timing performance, the timing residual, as defined in Section 7.1.2, is presented in Figure 55 for different bias voltages. No significant change of the timing residual can be observed. This is expected, if the timing residual for the different bias voltages is limited by the precision of the used setup, as discussed in Section 7.1.2, and
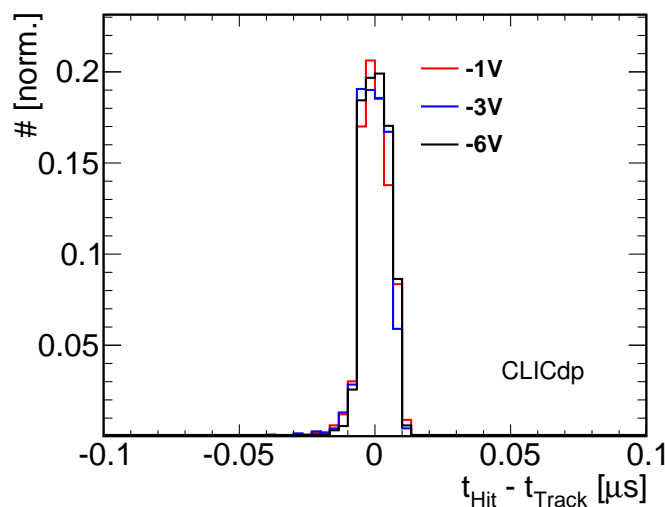
Figure 55: Timing residual for different bias voltages.

hints at the fact that the intrinsic timing resolution of the studied HR-CMOS process is well below the measured 5 ns. To conclude, a high bias voltage does not appear to be necessary to obtain a fast and efficient operation of the studied Investigator mini-matrix. However, a high voltage is necessary to achieve lower sensor capacitance resulting in a lower noise. As a consequence, a lower single-pixel threshold can be applied during the analysis and a larger cluster size and better spatial resolution can be achieved.

8. Summary

The investigator chip fabricated in a 180 nm HR-CMOS process has been characterised in laboratory and test beam measurements. The analysed data has been recorded for a mini-matrix with a pitch of 28 μm. A single point resolution of ∼ 6 μm has been determined. A timing resolution of ∼ 5 ns has been measured for various bias voltages, giving evidence for the fact that the measured timing resolution is dominated by the used setup. A measurement of the efficiency of > 99 % shows that the studied Investigator mini-matrix can be operated fully efficiently.

The observables have been studied with sub pixel precision, giving a more detailed understanding of the measured performance. Moreover, a threshold scan has been performed, showing that low threshold values of < 500 e$^-$ are favourable to be fully efficient and achieve optimal spatial resolution. A scan of the bias voltage further indicates, that higher bias voltages are favourable, due to lower sensor capacitance and thus a lower detector noise. This results in lower possible operation thresholds, giving a higher cluster size and better spatial resolution.

The measured efficiency and spatial resolution match well the requirements for the CLIC tracker. The presented results are used in a next phase of R&D as input for the design of a fully monolithic sensor for the CLIC tracker, incorporating also digital logic in the pixels. This sensor will also allow for a more refined assessment of the time resolution.

Acknowledgements

References

[1] M. Aicheler et al.,
A Multi-TeV Linear Collider Based on CLIC Technology: CLIC Conceptual Design Report,
tech. rep. CERN-2012-007, Geneva, 2012, DOI: `10.5170/CERN-2012-007`.

[2] L. Linssen et al., *Physics and Detectors at CLIC: CLIC Conceptual Design Report*,
tech. rep. CERN-2012-003, Geneva, 2012, DOI: `10.5170/CERN-2012-003`.

[3] P. Lebrun et al., *The CLIC Programme: Towards a Staged e+e- Linear Collider Exploring the
Terascale: CLIC Conceptual Design Report*, tech. rep. CERN-2012-005, Geneva, 2012,
DOI: `10.5170/CERN-2012-005`.

[4] M. J. Boland et al., CLIC and CLICdp collaborations,
Updated baseline for a staged Compact Linear Collider, tech. rep. CERN-2016-004,
Geneva, 2016, DOI: `10.5170/CERN-2016-004`.

[5] N. Alipour Tehrani et al., *CLICdet: The post-CDR CLIC detector model*,
CLICdp-Note-2017-001 (2017), URL: `https://cds.cern.ch/record/2254048`.

[6] A. M. Nurnberg, D. Dannheim, *Requirements for the CLIC tracker readout*,
CLICdp-Note-2017-002 (2017), URL: `http://cds.cern.ch/record/2261066`.

[7] B. Abelev et al., ALICE Collaboration,
Technical Design Report for the Upgrade of the ALICE Inner Tracking System,
tech. rep. CERN-LHCC-2013-024, 2013, DOI: `10.1088/0954-3899/41/8/087002`.

[8] C. Gao et al., *A novel source drain follower for monolithic active pixel sensors*,
Nuclear Instruments and Methods in Physics Research Section A **831** (2016), Proceedings of the
10th International Hiroshima Symposium 147, DOI: `10.1016/j.nima.2016.03.074`.

[9] A. Tehrani, *Test-beam measurements and simulation studies of thin pixel sensors for the CLIC
vertex detector*, PhD thesis, presented 13 Mar 2017, DOI: `10.3929/ethz-b-000164813`.

[10] J. W. van Hoorne, *Study and Development of a novel Silicon Pixel Detector for the Upgrade of
the ALICE Inner Tracking System*, PhD thesis, presented 24 Nov 2015,
URL: `https://cds.cern.ch/record/2119197`.

[11] W. Snoeys, *CMOS monolithic active pixel sensors for high energy physics*,
Nuclear Instruments and Methods in Physics Research Section A **765** (2014), Proceedings of the
9th International Hiroshima Symposium 167, DOI: `10.1016/j.nima.2014.07.017`.

[12] ANALOG DEVICES,
AD9249: 16 Channel 14-Bit, 65 MSPS, Serial LVDS, 1.8 V A/D Converter, 2013,
eprint: `http://www.analog.com/media/en/technical-documentation/data-sheets/AD9249.pdf`.

[13] M. Be et al., *Table of Radionuclides (Vol. 3 A = 3 to 244)*, Sevres, 2006, ISBN: 92-822-2218-7.

[14] T. Poikela et al., *Timepix3: a 65K channel hybrid pixel readout chip with simultaneous ToA/ToT
and sparse readout*, Journal of Instrumentation **9** 05 (2014) C05013,
DOI: `10.1088/1748-0221/9/05/C05013`.

[15] I. Rubinskiy et al., *EUTelescope. Offline track reconstruction and DUT analysis software.*
EUDET-Memo-2010-12 (2010), eprint: `https://www.eudet.org/e26/e28/e86887/e107460/EUDET-Memo-2010-12.pdf`.

[16] E. Belau et al., *Charge collection in silicon strip detectors*,
Nuclear Instruments and Methods in Physics Research **214** 2 (1983) 253, ISSN: 0167-5087,
DOI: `10.1016/0167-5087(83)90591-4`.

[17]   V. Blobel, C. Kleinwort, *A new method for the high-precision alignment of track detectors*, DESY 02-077 (2002), arXiv: `hep-ex/0208021`.

A. Pixel by pixel gain fluctuations

The mean values of Gaussian fits to the peak at $1639\,e^-$ in the ^{55}Fe-spectrum are presented for each single pixel. From Figure 56 up to Figure 58 results are shown for different bias voltages, showing a small pixel by pixel gain fluctuation in the order of a few percent.
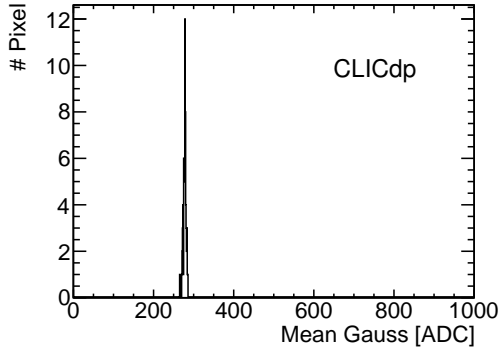

Figure 56: Mean values of Gaussian fits to single pixel spectra for $-1\,$V bias voltage.
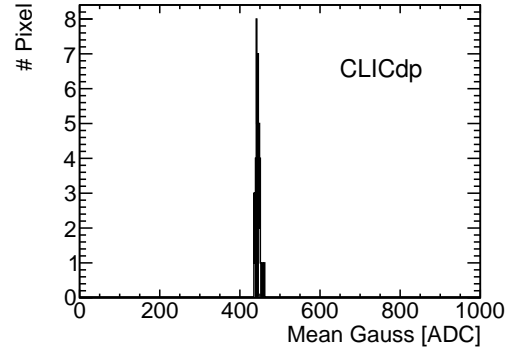
Figure 57: Mean values of Gaussian fits to single pixel spectra for $-3\,$V bias voltage.
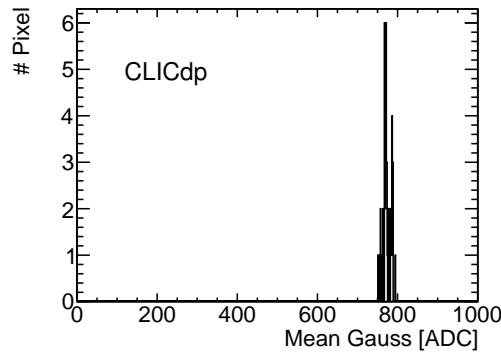

Figure 58: Mean values of Gaussian fits to single pixel spectra for $-6\,$V bias voltage.

B. Pixel by pixel noise fluctuations

The distribution of the single pixel noise before the calibration is presented in Figure 59 for different bias voltages [10]. Figure 59 shows the noise distribution during data taking (before the common mode noise correction, left plot) and as calculated in the analysis (after the common mode noise correction, right plot). The distributions show, that most of the noise values are similar for the different pixels, apart from a few outliers.

Figure 60 shows the noise for each pixel at different bias voltages after applying the calibration. The

---

[10]As discussed in Section 3, the noise is defined as the RMS of the amplitude fluctuations around the pedestal.
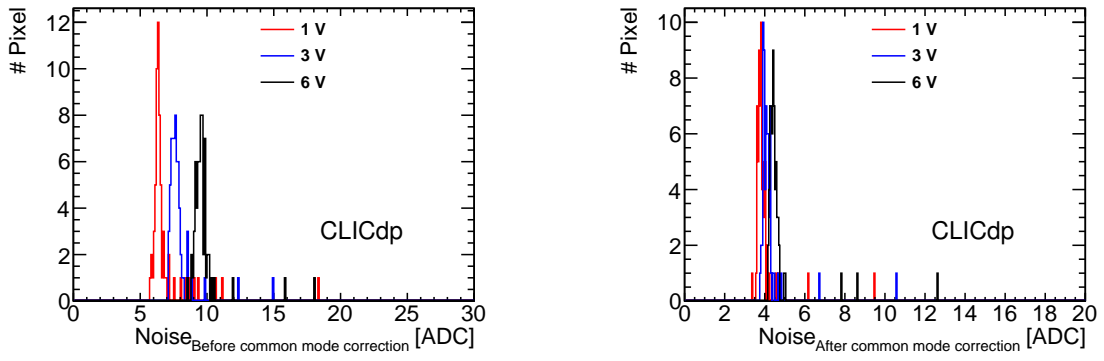
Figure 59: Noise before the calibration in units of ADC *before* (left) and *after* (right) the common mode correction.

noise distributions are displayed before the common mode noise correction (left plot) and after the common mode noise correction (right plot).
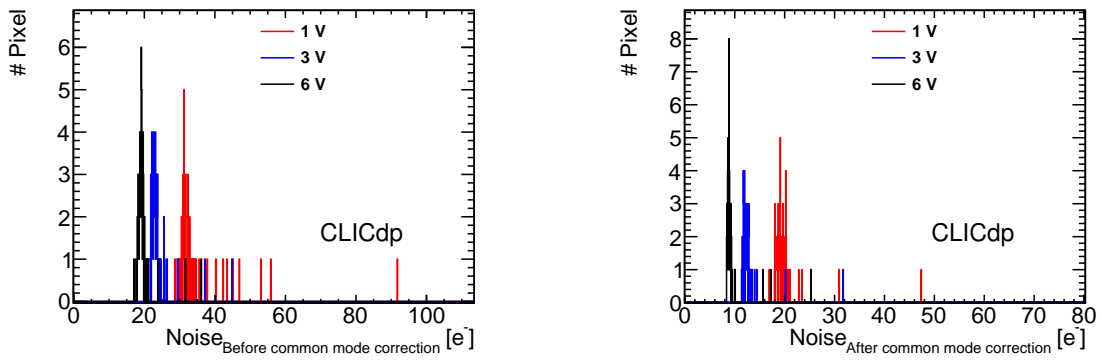

Figure 60: Calibrated noise in units of electrons *before* (left) and *after* (right) the common mode correction.